Spatial variations in the effective elastic thickness of the lithosphere in Southeast Asia

Xiaobin Shi, Jon Kirby, ChuanhaiYu, Alberto Jiménez-Díaz, JunfengZhao

PII: S1342-937X(16)30293-3
DOI: doi: 10.1016/j.gr.2016.10.005
Reference: GR 1690

To appear in: *Gondwana Research*

Received date: 1 April 2016
Revised date: 19 September 2016
Accepted date: 1 October 2016

Please cite this article as: Shi, Xiaobin, Kirby, Jon, ChuanhaiYu, Jiménez-Díaz, Alberto, JunfengZhao, Spatial variations in the effective elastic thickness of the lithosphere in Southeast Asia, *Gondwana Research* (2016), doi: 10.1016/j.gr.2016.10.005

Spatial variations in the effective elastic thickness of the lithosphere in Southeast Asia

Xiaobin Shi[a*], Jon Kirby[b], ChuanhaiYu[a,c], Alberto Jiménez-Díaz[d], JunfengZhao[a]

[a]Key Laboratory of the Marginal Sea Geology, South China Sea Institute of Oceanology, Chinese Academy of Sciences, 164, Xingang Xi Road, Guangzhou 510301,China

[b]Department of Spatial Sciences, Curtin University, GPO Box U1987, Perth, WA 6845, Australia

[c]University of Chinese Academy of Sciences, Beijing 100039, China

[d]Departamento de Geodinámica, Facultad de Ciencias Geológicas, Universidad Complutense de Madrid, 28040 Madrid, Spain

Abstract

As a proxy for long-term lithospheric strength, detailed information on lateral effective elastic thickness (T_e) variations can aid in understanding the distribution pattern of surface deformation and its response to long-term forces. Here we present high-resolution maps of spatial variations of T_e for the complex SE Asian region by analyzing the coherence of topography and Bouguer gravity anomaly data. We find that after considering the gravity deficit of less dense sediment, the recovered T_e maps are more representative of the geology, particularly in elongated rift basins. The results show that the T_e variation pattern in SE Asia, in general, agrees well with its tectonic provinces and major tectonic boundaries. The oceanic basins, the Indosinian suture zones between the Indochina and Sibumasu blocks, and the Makassar Strait are characterized by low T_e, while moderate and high T_e values are recovered in the Khorat plateau, West Burma, the Singapore Ridge, the Con Song Swell, Borneo, the northern Australian margin and the Molucca Sea. The T_e pattern in the south Indonesian margin is complicated by the approach and collision of oceanic plateaus and seamounts with the fore-arc region. The heterogeneous strength features are consistent with the complex assemblage of different tectonic units, and significant deformation during Cenozoic tectonic events. In the Indochina Peninsula, the extruded displacement during the India-Eurasia collision might have

* Corresponding author, E-mail: xbshi@scsio.ac.cn

been partitioned and absorbed by the combined mechanism of the extrusion and viscous tectonic models. As a result, the offshore displacements of the major strike-slip faults in the South China Sea are much smaller than originally assumed, thus having less effect on the development of the South China Sea than other mechanisms such as the slab pull of the proto-South China Sea. Since the displacement driven by the boundary tectonic forces has been greatly absorbed and decreased by subduction and deformation in the active margins and adjacent weak regions, the motion velocity of the interior regions is greatly lower than the boundary active margins, and they are largely free of seismicity and volcanism. Our results suggest that East Borneo might share a similar crustal basement, and represent a broad tectonic zone of the destroyed Meso-Tethys Ocean extending from West-Middle Java, through East Borneo to northern Borneo of the Sarawak and Sabah. The Indosinian zones between the Indochina and Sibumasu blocks might extend further southeastward across Billiton Island to offshore of southern Borneo, and the Singapore platform and SW Borneo might belong to the same block. The results also show that the internal load fraction *F* is high in the coastal area of South China, the northern margin of the South China Sea, and the coastal area of Indochina, which, in general, agrees with the distribution of a high-velocity lower crustal layer and Late Cenozoic basaltic rocks.

Keywords: effective elastic thickness; spectral methods; lithosphere structure; Southeast Asia; Continental deformation

1. Introduction

Mechanical properties of the lithosphere are of primary importance in controlling its response to long-term forces and, therefore, the temporal evolution and spatial configuration of the lithosphere (e.g., Tassara et al., 2007; Burov, 2011). Lithospheric strength can be measured by analyzing the resistance to vertical deformation (>10^5 year), which can be parameterized as flexural rigidity or, equivalently, its effective elastic thickness, T_e (Watts, 2001). The effective elastic thickness corresponds to the thickness of an idealized elastic beam or plate that would bend similarly to the actual lithosphere under the same applied loads (Watts, 2001), and primarily depends on parameters of power law creep, i.e., temperature, crustal thickness, fluid, lithologic variations, and to a lesser degree strain rate (Burov and Diament, 1995; Lowry and Smith, 1995;

Ranalli, 1997). Therefore, although T_e does not represent an actual depth to the base of the mechanical lithosphere, it could provide important insight into its rheology and state of stress, and could be used to improve our understanding of the relationship between tectonic styles, distribution of earthquakes and lithospheric rheology in various tectonic settings (Lowry and Smith, 1995; Tassara et al., 2007; Pérez-Gussinyé et al., 2007).

Southeast Asia (SE Asia), located in the southeastern part of the Eurasian Plate (Fig. 1), comprises a complex assemblage of allochthonous continental fragments, volcanic arcs, suture zones and marginal oceanic basins (e.g., Metcalfe, 2011; Hall, 2012). It is bounded by tectonically active margins which exhibit intense seismicity and volcanism. On the contrary, the interior of SE Asia is largely free of seismicity and volcanism. However, this tectonically quiet feature does not mean that the interior of SE Asia is a single homogeneous block (Hall and Morley, 2004; Takemoto et al., 2009; Yang et al., 2015). Therefore, a high resolution spatial variation map of T_e is necessary for understanding the tectonic formation variation, earthquake distribution, stress and strain transfer, and examining the different dynamic models proposed to explain large-scale tectonic structure in SE Asia (e.g., Tapponnier et al., 1982; England and Houseman, 1986). Since the strength contrast between different lithospheric domains could control the localization of deformation in response to tectonic forces (Tassara et al., 2007), a high-resolution T_e map might provide some valuable clues of the extension of block boundaries in regions which remain understudied due to difficulty of access, vegetation and climate (Hall and Spakman, 2015).

Spectral methods are one of the most commonly used methods to calculate the effective elastic thickness(Kirby, 2014). The cross-spectral analysis of gravity anomalies and topography permits assessment of the nature of isostatic compensation within a region, and has been widely applied to the estimation of lithospheric elastic effective thickness over a wide range of tectonic environments (e.g., Lowry and Smith, 1995; Swain and Kirby, 2006; Tassara et al., 2007; Perez-Gussinyéet al., 2007; Mao et al., 2012; Jiménez-Díaz et al., 2014). In the following sections, we first briefly introduce the wavelet method (Kirby and Swain, 2004; 2009; 2011) and data employed for estimating T_e, then present the high-resolution spatial variations of T_e and the fraction of the initial internal load in SE Asia. Finally, we examine the T_e variations in different tectonic provinces, and discuss the possible tectonic implications of the spatial variations of T_e and the internal load fraction.

2. An outline of Southeast Asian tectonics

SE Asia comprises a complex collage of continental fragments and marginal oceanic basins, which are connected through a series of volcanic arcs and suture zones (e.g., Metcalfe, 2011) (Fig. 1). It is bounded by the ongoing westward subduction of the Pacific Ocean and Philippine Sea, and the northward subduction system of the Indo-Australian plates. These continental lithospheric blocks, including Indochina, Sibumasu and West Burma, SW Borneo and East Java–West Sulawesi, were mostly rifted from Gondwana, transferred northward, and accreted together with Paleo-Asia by closure of different ages Tethyan oceans (e.g., Metcalfe, 2011; Hall, 2012). Between the Indochina and the Sibumasu blocks lie the Indosinian suture zones (the Changning–Menglian and Inthanon sutures in southwest China and Thailand, and the Bentong-Raub Suture in the Malay Peninsula) in the west, and the Permian and Triassic Thai-Malay Tin Granite Belt (Lincang Granitoid Batholith, Sukhothai, and East Malaya of the Malay Peninsula) in the east (e.g., Metcalfe, 2011). These sutures and granite belts represent the relic of the Devonian–Triassic Palaeo-Tethys Ocean and the products of associated subduction and post-collisional magmatism (e.g., Metcalfe, 2011). It was suggested that the sliver of the West Sumatra and West Burma Blocks was translated along a strike-slip fault from Indochina westwards to positions outboard of Sibumasu in the Triassic (Metcalfe, 2011). West Sumatra and West Burma are now separated from one another by the Andaman Sea. The SW Borneo Block is bounded to the north by the Lupar and Boyan zones (with the small Semitau Block between) and to the southeast by the Meratus and LukUlo sutures with East Java–West Sulawesi (Hall et al., 2008). With the Cenozoic collision of India-Eurasia, several of the major strike-slip fault zones, such as the Sagaing, Three Pagodas, Mae Ping, and Red River Faults were developed crossing the western study area (South China, West Burma, Sibumasu, and Indochina Blocks) when the crustal blocks bounded by these faults extruded laterally (Tapponnier et al., 1982; Morley, 2012). The strike-slip movement of the Sagaing fault might have resulted in the opening of the Andaman Sea in the Late Miocene (Metcalfe, 2011).

The eastern part of SE Asia is composed of a series of marginal oceanic basins and rift basins. Seafloor spreading of the South China Sea was developed at 30 Ma through 16 Ma (Taylor and Hayes, 1983; Briais et al., 1993; Li et al., 2014). It is generally agreed that there was southward

subduction of the Proto-South China Sea beneath northern Borneo during the early Tertiary (e.g., Hutchison, 1996; Hall et al.,2008; Morley, 2012; Hall and Spakman, 2015; Simons et al., 2007). The subduction of the proto-South China Sea ended in the Early Miocene when the Dangerous Grounds block-Reed Bank underthrusted northern Borneo (Morley, 2012), which was coincident with the termination of the seafloor spreading in the South China Sea. The remnant of the proto-South China Sea can now only be tracked along the Nansha trough. The Celebes and Philippine Sea were developed in a backarc setting with northward subduction of the Ceno-Tethys along from Sumatra to Halmahera, and the southward subduction of the Proto-South China Sea at the Sabah margin during the Eocene (Hall, 2012). At around 15 Ma, the subduction rollback of the Celebes Sea formed the Dent–Semporna–Sulu Arc and caused spreading of the Sulu Sea in a backarc setting. The development of Banda seas and volcanic arcs were associated with the northward subduction and subduction rollback of the Ceno-Tethys between the Australian northern margin and Asia in the Neogene (Hall, 2012). The Java trench evolves beyond 120˚E from the subduction zone to collision with the Australian plate along the Timor Trough (e.g., Pubellier et al., 2003). The collision resulted in a broadly deformed area and affects the entire Banda and Molucca region. The North Banda Sea was formed between 12.5 and 7 Ma and the South Banda Sea between 6 and 2 Ma (Hinschberger et al., 2005). The double subduction system between the two arcs was initiated at about 15 Ma, and the Molucca Sea has since been eliminated by subduction at both its eastern and western sides. The present-day Molucca Sea results from a collision between two opposed oceanic arcs: the Halmahera Arc to the east and Sangihc Arc to the west (Hinschberger et al., 2005). The Philippine Archipelago, forming the western boundary of the Philippine Sea plate, is limited by two oppositely dipping subduction zones: the Manila Trench to the west and the East Luzon Trough-Philippine Trench to the east. The Manila Trench connects with the Negros-Sulu-Cotobato trench system along the marginal basins (i.e., South China Sea, Sulu Sea and the Celebes Sea) on the eastern edge of the Eurasian Plate. These subduction zones continue on as collision zones in Taiwan, Mindoro, Panay and the Mindanao islands. The Eastern subduction system along the East Luzon Trough-Philippine Trench is widely believed to have initiated 3–5 Ma (Ozawa et al., 2004).

3. Method and data

3.1. Load deconvolution with the wavelet transform

Here we use a wavelet transform adaptation of Forsyth's (1985) method to estimate T_e (Swain and Kirby, 2006). Forsyth's method takes the observed Bouguer gravity anomaly and topography data, and attempts to reconstruct the surface and subsurface loads that initially flexed the plate during the most recent period of geological activity. The process is often referred to as 'load deconvolution' (Lowry and Smith, 1994; Kirby, 2014), and requires an estimated T_e value which is then varied until the coherence between the reconstructed initial loads matches the coherence between the observed Bouguer anomaly and topography data: this gives the T_e value for the data. The Bouguer coherence curve has a characteristic shape: at small wavenumbers (long wavelengths) it has values around 1, indicating high coherence between Bouguer anomaly and topography and suggestive of isostatic compensation; at high wavenumbers (short wavelengths) it has values around 0, indicating low coherence between Bouguer anomaly and topography and suggestive of mechanical support. The wavenumber at which the coherence curve rolls over from 1 to 0 is called the transition wavenumber: if this wavenumber is small (long wavelength) then the plate is strong (high T_e) as it can adequately support large loads without deflecting much; but if the transition wavenumber is high (short wavelength) then the plate will have alow T_e.

The procedure just described is typically performed via least squares inversion– though other methods exist (Kirby, 2014)– so that $T_e$is estimated as an inversion parameter, with corresponding errors.

Along with the T_e values, the load deconvolution method also provides the wavenumber-dependent initial loading ratio, $f(k)$, obtained from the reconstructed initial loads (Forsyth, 1985); it is the ratio of the initial internal to initial surface load, in the wavenumber domain. The loading ratio is typically presented as a single value though, being its value at the wavenumber corresponding to the coherence transition wavenumber; for this reason, maps of the spatial variation of f often correlate with maps of T_e variation, since both quantities are dependent upon the coherence transition wavenumber (e.g., Tassara et al., 2007). However, as Forsyth (1985, p. 12,629) notes, "The estimate of elastic thickness from coherence is not very sensitive to uncertainty in f."This is fortunate because errors in $f(k)$ are hard to estimate in the load deconvolution method. Whereas T_e is an inversion parameter solved for by least squares methods, the loading ratio is not

an independent inversion parameter in load deconvolution, and so its errors cannot be estimated using this approach.

The loading ratio, *f*, is sometimes represented as an internal load fraction, *F* (McKenzie, 2003) because *F* varies between 0 and 1, whereas *f* varies between 0 and ∞. The *F* parameter is defined as the ratio of the initial internal load amplitude to the total amplitude of both initial loads, and is wavenumber-dependent. Purely surface loading gives $F = 0$, and purely internal loading gives $F = 1$.

We calculate the coherence using the fan wavelet transform with high spatial resolution (Kirby and Swain, 2004, 2011). The wavelet transform is a space-domain convolution of a range of scaled and rotated complete Morlet wavelets with a signal, here the Bouguer anomaly and topography. For a 2D space-domain (**x**) signal g(**x**) with Fourier transform G(**k**) where **k** is 2D wavenumber, its wavelet coefficients are computed in the wavenumber domain via $\tilde{g}(s,x,\theta) = F^{-1}[G(k)\hat{\psi}_{s\theta}(k)]$, where *s* and θ are the scale and azimuth of the Morlet wavelet respectively, $\hat{\psi}_{s\theta}(k)$ is the Fourier transform of the wavelet at a certain scale and azimuth, and F^{-1} is the inverse 2D Fourier transform. The scale is mapped to wavenumber by the peak wavenumber method (e.g., Kirby, 2005). Rather than the coherence, we compute the observed SRC (the square of the real part of the coherency) at each grid node, given by Kirby and Swain (2009) as

$$\Gamma_R^2 = \frac{(\mathrm{Re}\langle \tilde{g}\,\tilde{h}^* \rangle)^2}{\langle \tilde{g}\,\tilde{g}^* \rangle \langle \tilde{h}\,\tilde{h}^* \rangle} \qquad (1)$$

Where $\tilde{g}$ and $\tilde{h}$ are respectively the wavelet transforms of the Bouguer gravity anomaly and topography, * indicates complex conjugation, and bracket indicates averaging over azimuth θ over the upper quadrants only (i.e. over 180º) (Kirby and Swain, 2004). Then T_e is estimated at each space-domain grid node by minimizing the misfit between the observed SRC with that predicted from the loading and flexure of a thin elastic plate (the predicted SRC) using the load deconvolution method, as described above (Forsyth, 1985; Kirby and Swain, 2011).

The complete Morlet wavelet is used to give a better space-domain resolution of wavelet coefficients. In the wavenumber domain, the mother wavelet equation is $\psi(\mathrm{K}) = e^{-|\kappa-\kappa_0|/2} - e^{-(|\mathrm{K}|^2+|\mathrm{K}_0|^2)/2}$, where $|\mathbf{k}_0|$ is the central wavenumber of the Morlet wavelet.

$|\mathbf{k}_0|$ governs the resolution of the wavelet in the space and wavenumber domains; larger values of $|\mathbf{k}_0|$ give better wavenumber resolution but poorer spatial resolution, and vice versa for smaller values. Kirby and Swain (2011) found that owing to the better wavenumber-domain resolution, values of >5 could give more accurate absolute T_e estimates if the tectonic province is large and contains a relatively uniform T_e, while if detailed T_e structure and/or accurate relative T_e differences are required, then values of <3.5 are more likely to be useful. In this study, to obtain a comprehensive pattern of T_e variations for our complex study area, we present the T_e results of $|\mathbf{k}_0|$ = 2.668 and 3.773.

While lower-$|\mathbf{k}_0|$ wavelets have a demonstrably better space-domain resolution than their higher-$|\mathbf{k}_0|$ counterparts (e.g., Addison et al., 2002), quantifying this resolution in terms of the relative size and magnitude of elastic thickness anomalies is difficult. First, an elastic plate with a uniform elastic thickness possesses a characteristic flexural wavelength which determines the wavelength of the flexural depression under application of a point load (e.g., Watts, 2001). Swain and Kirby (2003) give an approximate formula for the flexural wavelength of $\lambda \approx 29 T_e^{3/4}$. In synthetic testing of the wavelet method, Kirby and Swain (2008) found that relative T_e differences between adjacent provinces will be underestimated when the T_e anomaly is narrow compared to its flexural wavelength. This happens because the spatial diameter of the wavelet is greater than the anomaly width, and information about T_e is smeared across provinces. When low-$|\mathbf{k}_0|$ wavelets are utilized, their spatial diameter is less than that of a higher-$|\mathbf{k}_0|$ wavelet for a given T_e, so there will be less smearing. In further synthetic tests, Kirby and Swain (2011) showed that, when using a $|\mathbf{k}_0|$ = 2.668 wavelet, T_e anomalies with widths as low as 100 km could be resolved albeit with reduced relative magnitude. With real data, however, this resolution could be degraded somewhat since their synthetic models contained no non-flexural gravity signals.

The two values, $|\mathbf{k}_0|$ = 2.668 and 3.773 were chosen for their relatively good spatial resolution since the focus of this study concerns a regional-scale tectonic interpretation of T_e results, rather than determination of a gross or general T_e value for the region where a higher $|\mathbf{k}_0|$ value (e.g. 5.336) would be more appropriate. As mentioned above, low-$|\mathbf{k}_0|$ wavelets have good spatial resolution but poor wavenumber resolution: the 2.668 wavelet would be better able to resolve T_e variations, while the 3.773 wavelet results would act as gross control of the T_e values recovered by the 2.668 wavelet through their more accurate estimation of the coherence transition wavenumber.

3.2. Input Data

The topography and bathymetry grid data was extracted from the GEBCO_08 Grid of GEBCO digital atlas (http://www.gebco.net) (British Oceanographic Data Centre, 2008). The GEBCO_08 Grid is a continuous terrain model for ocean and land with a spatial resolution of 1 arc-minute. To treat mixed land and marine environments, we followed Stark et al. (2003) and Kirby and Swain (2008), and scaled ocean bathymetry *h(x)* to an equivalent topography $h(x) = (\rho_{uc} - \rho_w)h(x)/\rho_{uc}$ prior to Fourier transformation. Values of the densities are given in Table 1. Thus, we can compute T_e for the whole area (in one run) using only the land-loading equations, and avoid T_e discontinuities at the coastlines.

The free-air gravity anomaly data of $2.5' \times 2.5'$ are taken from the Earth Gravitational Model EGM2008 (Pavlis et al., 2012) which is performed using the tide-free version of EGM2008 to degree 2160. EGM2008 provides a free-air gravity anomaly database of ~20 km mean resolution that exploits all of the latest data and modeling for both land and marine areas worldwide. The free-air gravity anomaly data was then converted to complete Bouguer gravity anomaly using the FA2BOUG software (Fullea et al., 2008) with the topography data from GEBCO_08 grid for terrain corrections and a reduction density of 2670 kg m^{-3}. The free-air and complete Bouguer gravity anomaly of the study area are shown in Fig. 2.

However, the spectral methods for T_e generally ignore the density difference between sediment and basin basement, which might cause significant T_e biases in regions where the sediment is extremely thick. In our study area, there are some very deep sedimentary basins (such as the Yinggehai, Qiongdongnan, Pearl River Mouth and Malay basins; Fig. 1). Compared with the basin basement, the thick and less dense sediments cause a prominent negative gravity anomaly Δg_s (e.g., Braitenberg et al., 2006). To eliminate the effect due to the less dense sediment, we use the method of Rao and Babu (1991) to calculate the negative gravity anomaly Δg_s at sea level caused by the sediment in the marine area, which is obtained from the most recent $5' \times 5'$ sediment thickness grid (Total Sediment Thickness of the World's Oceans and Marginal Seas, Version 2, http://www.ngdc.noaa.gov/mgg/sedthick/) (Whittaker et al., 2013). To avoid the edge effects of

gravity anomaly calculation, we used sediment thickness data over a slightly larger area than our study area, ranging from 85˚E to 145˚E longitude and from 25˚S to 30˚N latitude. Since the sediment thickness data grid contains a blank area (no sediment thickness data) in the northeastern South China Sea, we replaced the blank area with published sediment thickness maps (e.g., Lin et al., 2003). Fig. 3 shows the maps of sediment thickness and the negative gravity anomaly Δg_s, whose absolute value could be larger than 70 mGal in places with thick sediment. Then we calculated the sediment-corrected Bouguer gravity anomaly by $\Delta g_{Bs} = \Delta g_B - \Delta g_s$. Following the method of converting water depth to equivalent rock load, we convert the sediment thickness to equivalent rock load and obtained a new equivalent topography $h(x) = (\rho_{uc} - \rho_w)h(x)/\rho_{uc} + (\rho_{uc} - \rho_s)l(x)/\rho_{uc}$, Where ρ_s and $l(x)$ are the sediment density and thickness, respectively.

In the calculation of the predicted SRC, the load deconvolution method described above requires knowledge of the crustal structures, and the internal loading depth. For the crustal structures, we use the 2°× 2° CRUST2.0 model (Bassin et al., 2000). Since wide-angle reflection seismic data reveal a high velocity layer at the bottom of the lower crust on the northern margin of the South China Sea (e.g., Nissen et al., 1995; Lester et al., 2014; Xia et al., 2014 and references therein), following the original formulation of Forsyth (1985), we assumed that the initial internal loading occurs at the Moho. We also tested placing the internal load at different surfaces (the upper/middle crust, the middle/lower crust, and Moho surface), with constant density differences or density structures of the CRUST2.0 model, and obtained similar spatial T_e variations. Though there is a trade-off between T_e and the assumed depth of internal load when modeling the observed SRC, the T_e maps calculated with different internal load depths all show similar variation patterns (Pérez-Gussinyé et al., 2007). Just like Kirby and Swain (2009), we also concluded that the T_e results seem insensitive to small changes of Moho depth or density (Tassara et al., 2007). Errors on the SRC were calculated using the jackknife method of Kirby and Swain (2013), with T_e errors obtained from Brent's method (Press et al., 1992).

All the topography, gravity and crustal data were projected into a planar Cartesian coordinate system using the Mercator projection, and then resampled onto 20 km grids, and were mirrored about their edges prior to Fourier transformation. In order to remove the gravity edge effect that

arises when performing the terrain correction (e.g., Fullea et al., 2008), the final study area is slightly smaller than the computation area which extends from 25ºS to 30ºN in latitude, and 85ºE to 145ºE in longitude. The final study area extends from 20ºS to 25ºN in latitude, and 90ºE to 140ºE in longitude, and in its projected form has dimensions of 5780 km (easting) by 5260 km (northing) on a 20 km grid spacing.

4. Results

4.1. Sediment-uncorrected and sediment-corrected T_e maps

As mentioned, since the spectral methods for T_e generally ignore the density difference between sediment and basin basement, thick sediments, which can produce significant negative gravity anomalies, might have a strong influence on T_e estimates. Figs 4 and 5 present the recovered T_e results from $|\mathbf{k}_0|$ = 2.668 and $|\mathbf{k}_0|$ = 3.773, using both the sediment-uncorrected and the sediment-corrected gravity anomaly and topography data. Prominent differences occur in the elongated regions where very thick sediments have been deposited. Here the sediment-corrected T_e values are significantly smaller than the sediment-uncorrected results, suggesting that the thick, less dense sediment affects the T_e results. For example, there is a marked high T_e zone (> 60 km) along the NW trending Malay Basin in Fig. 4a, while the high T_e values are replaced with T_e of <20 km in the sediment-corrected T_e map (Fig. 4b). Similar T_e changes are also present in the Yinggehai Basin, northwest of the South China Sea. Both basins are elongated rift basins related to the motion of strike-slip faults, and are filled with Cenozoic sediment thicker than 14 km. However, high T_e values are generally incompatible with rifted basins, which are typically characterized by low T_e values (e.g., Watts, 2001; Clift et al., 2002), suggesting that a model in which sediments are accounted and corrected for is preferable. Furthermore, by analyzing the tectonic subsidence and gravity modeling of the Malay and Penyu Basins, Madon and Watts (1998) suggested that the T_e values in the center of the Malay basin are very low (T_e = 0 km), and about 12 km in the Panyu Basin, results which agree with our sediment-corrected T_e results.

Therefore, since the sediment-corrected model is a more faithful representation of the real Earth in this region, and since our sediment-corrected T_e results agree better with geological expectations and with independent control than do the uncorrected results, we use the sediment-corrected T_e maps in the following analyses.

4.2. T_e results

Figs 4b and 5bshow the sediment-corrected T_e estimates in the SE Asia of $|\mathbf{k}_0|$ = 2.668 and $|\mathbf{k}_0|$ = 3.773, respectively. We limit the color scale to a maximum T_e of 120 km. The T_e estimates from different $|\mathbf{k}_0|$ values vary in their absolute values and in the short wavelength variation. The small $|\mathbf{k}_0|$ gives a wider T_e range and smaller scale variations than the large $|\mathbf{k}_0|$ value. Nonetheless, their overall T_e variation patterns look very similar, and the average T_e values over the grid (mean of 28 km with a standard deviation of 27 km using the 2.668 wavelet, and mean of 30 km with a standard deviation of 26 km using the 3.773 wavelet) agree with each other. Thus, when used together both T_e maps show a comprehensive pattern of T_e variations for the complex study area.

Figs 4 and 5 show several incidences of T_e values changing by large amounts over a short spatial interval, giving a high T_e gradient. This phenomenon is often observed in studies where T_e is estimated by inverse spectral methods and is not limited to the wavelet method (e.g., Pérez-Gussinyé et al., 2009; Jiménez-Díaz et al., 2014). Fig. 6 shows a cross-section through the wavelet Bouguer SRC (coherence) over a profile shown in Fig. 5b. At around 1600-2000 km (Banda Sea) along the profile, T_e abruptly changes from ~55 km to ~5 km with an apparent infinite gradient (Fig. 6a), and this is reflected in the predicted coherence (Fig. 6c) from which T_e is derived. However, while the observed coherence (Fig. 6b) exhibits a rapid change from low to high coherence, this change is not discontinuous. In other words, although T_e does change rapidly in this region, its apparent infinite gradient is an artefact of the inversion. The rapidity of the change in the observed coherence will depend, for wavelets, on the value of $|\mathbf{k}_0|$.

To evaluate the effect of the presence of topographically unexpressed internal loading, known as “gravitational noise” on the T_e results (McKenzie and Fairhead, 1997; McKenzie, 2003; Kirby and Swain, 2009), we use the model-noise identification method of Kirby and Swain (2009) to calculate the normalized free-air squared imaginary coherency (SIC). This quantity contains information about out-of-phase harmonics in the free air anomaly and topography signals which are not modelled by Forsyth’s (1985) method. Such uncorrelated signals could indicate the presence of “model noise” which would contaminate inversion of the Bouguer SRC if it occurred at wavelengths close to the Bouguer coherence transition wavelength. Therefore, following Kirby and Swain (2009), we present the T_e results of $|\mathbf{k}_0|$ = 2.668 and $|\mathbf{k}_0|$ = 3.773 (Fig. 7) in which we mask out

the regions where the maximum value of the normalized free-air SIC $\overline{\Gamma}^2_{F,I} > 0.5$. The load-deconvolution method could bias T_e in these regions masked in grey, where the corresponding noise levels are high. As pointed out by McKenzie and Fairhead (1997), McKenzie (2003) and Kirby and Swain (2009), this problem can occur in regions of subdued topography, and often affects areas where the coherence method indicates high T_e. However, though Fig. 7shows that "gravitational noise" does exist in the study area, the marked regions of recovered high T_e values lie mainly in part of the northern Australian margins and the Java subduction system. Note that while large "gravitational noise" indicates a failure of the load-deconvolution method (e.g., Forsyth, 1985; Kirby and Swain, 2009), it does not necessarily imply that the lithosphere is weak (Audet and Burgmann, 2011).

Various methods have been applied to estimate T_e values in this part of the study area. These methods include the cross-spectral analyses of periodogram spectra (Su, 2012), the multitaper coherence method (Nair et al., 2011; Chen et al., 2013), the wavelet method (Swain and Kirby, 2006; Ratheesh-Kumar et al., 2010; Mao et al., 2012), the convolution method (Braitenberg et al., 2006), and forward modeling methods by recovering the observed gravity and topography data in the space domain with thin elastic plate flexure (e.g., Madon and Watts, 1998; Clift et al., 2002; Lin and Watts, 2002; Mouthereau and Petit, 2003; Shi et al., 2005; Bry and White, 2007; Hall et al., 2009). These existing studies focus on the South China Sea, Sunda margin, Indochina, and the Makassar Strait between the Borneo and the Sulawesi islands. In general, our results agree with these existing T_e estimates.

4.2.1. T_e in continental blocks

On the whole, the T_e variations in SE Asia agree well with its tectonic provinces. Figs 4b and 5b show that the study area is heterogeneous in rheological strength, and some isolated strong subregions are surrounded by weaker zones or regions. Along the Indosinian suture zones and the Permian through Triassic Thai-Malay Tin Granite Belt (Sukhothai Arc) between the Indochina and Sibumasu blocks (Metcalfe, 2011), there is a prominent nearly N-S trending weak zone (T_e< 20 km) extending from the Red River fault zone to the Malay Peninsula, which agrees well with Chen et al. (2013). The weak zone separates the Indochina Block from the western blocks of the Sibumasu and

West Burma. Besides this weak zone, the Indochina Block is also limited by two NW-trending weak fault zones, one along the Mae Ping Fault zone in its southwest (MPF in Fig. 1) and the other along the Red River Fault Zone in its northeast (RRFZ in Fig. 1). Similar to Chen et al. (2013), our results show that the Khorat plateau in the center of the Indochina Blockhas a strong lithosphere with T_e of 30-50 km. The Khorat Plateau Basin is the largest Mesozoic red bed basin in the central part of the Indochina. Its rigid nature has been confirmed by geological observations (e.g. Morley, 2012), palaeomagnetic data (Takemoto et al., 2009; Singsoupho et al., 2014), seismic tomography data (Li et al., 2006; Yang et al., 2015), and geothermal data (Yu et al., 2017; Fig. 8). The thermal lithosphere thickness derived from S-wave velocity data in the Khorat Plateau is 10-15 km larger than the surrounding area (Yu et al., 2017), and the surface heat flow is relatively low (50-60 mW/m^2) (Fig. 8), suggesting that the lithosphere in the Khorat Plateau is relatively cold and viscous compared to its surroundings.

In the west, the Sibumasu Block is separated from the West Burma Block by a dextral strike-slip zone (Fig. 1). Fig. 5b shows that the southern Sibumasu Block is much weaker than West Burma. The thinner (about 10-30 km thinner) thermal lithosphere thickness in the Sibumasu Block than West Burma (Yu et al., 2017) might be responsible for this weakness. Fig. 5b shows that there is a surprisingly elongated strong region with T_e> 50 km trending NWand across the West Burma and Sibumasu Blocks. Just to the east of the high T_e region, the northern segment of the Indosinian suture zones, the Changning–Menglian suture zone and the Lincang Granitoid Batholith are all displaced southeastward along the Lancang and Mengxing strike-slip faults (Fig. 9a). Although the two faults currently have right lateral and left lateral movement, respectively, geological observations suggest that the senses of the two faults were opposite during the Oligocene–Miocene (Lacassin et al., 1998; Wang et al., 2014). If the high T_e feature is correct, the southeastward extrusion of this region due to the India-Eurasia collision can explain the strike-slip movement of these faults and the resulted offset of the suture zone during the Oligocene–Miocene.

Borneo is characterized by moderate T_e. Fig. 5b shows that besides the Schwaner Block in the SW Borneo, which is composed of Palaeozoic metamorphic rocks, the East Borneo is characterized by a moderate T_e of 20-40 km. The stronger eastern Borneo is bounded by the weaker Makassar Strait. The T_e in the Makassar Strait is lower than 20 km, which is consistent with the result of Hall et al. (2009). Interestingly, our results show that in north Borneo, there are two strong regions which

might relate to the change of the structure line of the Interior Highland (Fig. 9b). One stronger region is in the southwest of the Tinjar Line. Just around the Tinjar Line there is a large dextral oroclinal bend of the Interior Highlands fold-thrust belt (Upper Cretaceous–Eocene Rajang-Crocker Group) (Cullen, 2014). The other stronger region lies in northeast Borneo (Sabah). The Interior Highlands fold-thrust belt again changes from nearly E-W trending in the west to NE trending in northeast Borneo. The two stronger regions might have behaved as rigid bodies, just like an anchor or an indenter, and resulted in the bending of the southward fold-thrust belt during the subduction of the proto-SCS and sequential orogeny.

T_e values in the Sunda shelf are generally lower than 20 km except for the Singapore platform, the Con Song Swell and the southern Java Sea (Fig. 5b). Though the basement of the gulf of Thailand might be Palaeo/Mesozoic crystalline/metamorphic basement, due to significant Cenozoic rifting, the T_e values of 10-20 km in the gulf suggest that the lithosphere has been greatly weakened. The Singapore platform is the strongest region of the Sunda shelf. Just to the north of the Singapore platform and SW Borneo, there is a weak zone along the Lupar Line extending from the coast of western Sarawak towards Natuna Ridge. The Lupar line is thought to be a significant suture zone between the Luconia block and west Borneo (e.g., Hutchison, 1996; Fyhn et al., 2009).

4.2.2. T_e in oceanic crust

Generally, following its creation at a spreading centre, oceanic lithosphere becomes more and more rigid as the plate cools, unless other events, such as thermal reheating and rejuvenation of the lithosphere, and an increase in curvature due to fracturing and faulting of deformed lithosphere, act to reduce its strength (Watts, 2001; Pérez-Gussinyé et al., 2008; Burov, 2011). However, it is worth to mention that T_e recovered by the methods related to thin plate flexure modeling primarily represents oceanic lithosphere strength at the time of loading, not necessarily its current actual strength (Watts, 2001). If there has been neither volcanism nor sedimentation since its creation, T_e represents the strength at the time of oceanic crust formation (and hence is very low) (Pérez-Gussinyé et al., 2008).

Cenozoic marginal seas in our study area are characterized by T_e values lower than 20 km, particularly in most of the South China Sea (spreading during 32-15.5 Ma), the Banda Sea (12.5-2 Ma), the Sulu Sea (the early Miocene or 35–30 Ma), and the Andaman Sea (<15 Ma) where the T_e

values are even lower than 10 km. In the South China Sea, most of the continental slope areas, oceanic area and the continental blocks such as the Xisha-Zhongsha Block (Macclesfield Bank) and Nansha Block (Reed Bank and Dangerous Grounds) show very low strength (T_e< 10 km), which agrees well with the results of Clift et al. (2002), Shi et al. (2005), Braitenberg et al. (2006), Mao et al. (2012), Su (2012) and Chen et al. (2013). T_e in the Taixi foreland basin to the west of Taiwan is in the range of 10-20 km, which also agrees well with the results of Lin and Watts (2002) and Mouthereau and Petit (2003). However, similar to our sediment-uncorrected results, the T_e values of Mao et al. (2012) and Chen et al. (2013) are much higher than our sediment-corrected results in the northern shelf of the South China Sea and the Gulf of Thailand (Fig. 4, Fig. 5), suggesting that their results might be affected by the thick, less dense sediments. The T_e pattern of the West Philippine Sea plate shows somewhat complex behavior. There is a low T_e zone of <10 km along the north-south trending Kyushu-Palau Ridge. The Kyushu-Palau Ridge is a remnant intra-oceanic arc that was active in the Eocene and Oligocene (42-29 Ma). The low T_e might represent the lithospheric strength when the arc was active. The northern West Philippine Basin, which is a Mesozoic arc terrene, was impacted by the Oki-Daito mantle plume at ca. 36 Ma (Ishizuka et al., 2013). The estimated low T_e of <10 km might represent the lithospheric rejuvenation strength due to the intensive magmatic activities.

4.2.3. T_e in subduction and collision systems

The strength of the Indonesian margin shows a relatively complex pattern. Along the Sunda trench (Sumatra and Java), the incoming oceanic plate becomes weaker when approaching the trench axis (Fig. 4b), which might be caused by the development of bending faults and plate bending (increased curvature) before subduction (Burov, 2011). However, since the incoming plate is topographically rough, with oceanic plateaus and seamounts (such as the Roo Rise), the T_e pattern in the subduction system, particularly in the southern Sumatra Trench and Java trench, is complicated by the approach and collision of oceanic basement relief with the fore-arc regions. Our analysis uses a continuous elastic plate as its model, whereas subduction systems, especially young, active ones, may be better modeled using a broken plate model (e.g., Watts, 2001). This is not possible using spectral methods, however, so we note that, while T_e might be underestimated by using a continuous plate (e.g., Karner and Watts, 1983), the error should not be large (Lowry and Smith, 1995).

Alternatively, the relatively high T_e values in the fore-arc regions suggest that the coupling between the over-riding plate and the subducting plate is strong (Perez-Gussinyé et al., 2007). Our recovered T_e values and complex pattern resemble the results of Bry and White (2007) and Ratheesh-Kumar et al. (2010). The lower T_e values recovered by Nair et al. (2011) for the entire Indonesian continental margin might be attributed to the small windows they used. However, Figs 4b and 5b show that T_e does not decrease from the forearc to the volcanic arcs of Sumatra and Java, where heat flow is higher than 80 mW/m^2 (Fig. 8). The grey regions in Fig. 7 show that the moderate T_e of 30-50 km in these regions might be biased by gravitational noise.

In the southeast of our study area, the T_e variation shows a bimodal pattern. Two strong and rigid regions of T_e> 50 km weaken rapidly to the regions of T_e< 20 km (Fig. 5b). Fig. 5b shows that the lithosphere in northern Australia is of very high strength with T_e> 70 km, which is consistent with the result of Swain and Kirby (2006). To the east of 120˚E,the strong and rigid northern Australian continent collides with the Banda Arc along the Timor Trough. Behind the Banda Arc lies the weak Banda Sea. Since the cessation of subduction at the Timor Trough, the continuing northward displacement of the Australian Plate (at a rate of about 7.5 cm/yr with respect to Eurasia) was mainly consumed by intra-arc shortening and thrust faulting during the Pleistocene (Hinschberger et al., 2005; Simons et al., 2007). The other prominent high T_e region is the Molucca Sea. The Molucca Sea Plate is subducting both to the southeast in the Halmahera subduction zone and to the northwest in the Sangihe subduction zone (Fig. 1), and the Sangihe and Halmahera arcs have begun to collide (Hinschberger et al., 2005). In subduction zones, where the upper plate and the downgoing plate are in contact, the measured effective elastic thickness can be expected to have contributions from both the upper plate and the subducted slab (Perez-Gussinyé et al., 2008). The high T_e suggests that the coupling between the overriding plates and the subducting plate might be very strong (Burov and Diament, 1995; Perez-Gussinyé et al., 2008). Tomography data show that the high P-wave velocity anomaly can extend to 150 km depth beneath the Molucca Sea (Huang et al., 2015). The strong lithosphere in the Molucca Sea is close to the high T_e region of the Palau Basin whose oceanic age is approximately 59 to 56 Ma (Hilde and Lee, 1984).

The T_e in the Philippine archipelago is lower than in the Sunda Subduction System. The Philippine archipelago is a broad convergence zone characterized by opposing subduction on the east and west sides. The T_e values are generally lower than 20 km.

5. Discussion

5.1. T_e and tectonic models

It is generally agreed that the ongoing convergence between the Indian and Eurasian plateshas driven the Cenozoic continental deformation in West Burma and the Indochina Peninsula(e.g., Tapponnier et al.,1982; Morley, 2012; Metcalfe, 2011). Two typical tectonic models have been advanced to account for the nature of the Cenozoic continental deformation. The extrusion tectonic model proposes that the convergence has driven the Indochina Peninsula to extrude southeastwards several hundred kilometers through a series of major strike–slip fault zones, and the huge displacement along the left-lateral Red River Faults during the Late Eocene through the Miocene has resulted in the opening of the South China Sea (e.g., Tapponnier et al.,1982; Briais et al., 1993).In contrast, the viscous tectonic model (England and Houseman, 1986) proposes that the continental lithosphere behaves as a 'thinviscous sheet', which deforms by diffuse crustal thickening over a wide lateral area and then by strike-slip faulting in the shallow crust. Our results show that the Indochina Peninsula is heterogeneous in rheological strength, and the strong central Indochina, with a stronger core of the Khorat Plateau, is surrounded by broad and linear weak zones. These weak zones extend along the major strike–slip fault zones (the Red River, Mae Ping and Three Pagodas), and the Indosinian suture zones between the Indochina Block and the Sibumasu Block. The southern Sibumasu Block is also characterized by low strength (T_e<20 km). Although West Burma is now characterized by high T_e, the Indo-Burma Ranges of West Burma might have been weaker when it was active margin. In response to the tectonic forces from the India–Eurasia collision zone, these weak regions, especially those close to the collision front, might have behaved as 'thinviscous sheet', and deformed significantly by extensive folding, thrusting, and strike-slip faulting. With the further indentation of rigid India into Asia, the internal shortening deformation in these weak zones has propagated northwards. As a result, elevated topography (high mountains) (Fig. 1), thickened crust, and intensive folded and thrusted Palaeocene–Oligocene sedimentary rocks can be seen in Myanmar, Northern Thailand, Laos and Yunnan (Searle and Morley, 2011 and references therein), and earthquakes occur more frequently in the northern Indochina Peninsula than in its southern and eastern parts (Simons et al., 2007; Tang and Zheng, 2013). In the southern weak regions, with the change from transpressional-dominated deformation to predominantly extensional

deformation, the later intense erosion and extension might have greatly thinned the crust which had been thickened during earlier compressed deformation, and deep rifted basins began to develop first in the Gulf of Thailand (Eocene-Middle Miocene), then onshore central Thailand (Late Oligocene-Late Miocene) (Searle and Morley, 2011).

By analyzing seismic reflection data, Morley (2013) revealed that these major strike–slip fault zones (the Red River, Mae Ping and Three Pagodas) have changed into strongly splaying tip geometries and died out after passing into offshore extensional provinces (the Yinggehai Basin and Gulf of Thailand).Morley (2013) concluded that the areas of the fault tips associated with faults of potentially >100 km displacement, and the Red River fault zone could not transfer displacement onto the South China Seas spreading centre. Combined with other geological evidence, many models on the South China Sea (e.g., Taylor and Hayes, 1983; Hutchison, 1996; Hall et al., 2008) employ slab pull of the Proto-South China Sea rather than the extrusion tectonic model as the primary driving force for the opening of the South China Sea. Tran et al. (2014) also found that the Cenozoic deformation is weak in the weak coastal area of Middle Vietnam (Fig. 5b). Therefore, although the western Indochina Peninsula has been extruded southeastwards several hundred kilometers during the India-Eurasia collision, the displacement might have been partitioned and absorbed by the combined mechanism of the extrusion and viscous tectonic models. As a result, the eastwards and southwards displacement gets smaller and smaller, and the offshore displacements of the major strike-slip faults in the South China Sea are much smaller than originally assumed (e.g., Tapponnier et al. 1982), thus having less effect on the development of the South China Sea than other mechanisms such as the slab pull of the proto-South China Sea.

5.2. T_e and tectonic zones

SE Asia is geologically a particularly complex region and remains relatively understudied because of difficulties of access, vegetation and climate (Hall and Spakman, 2015). Due to most of East Borneo covered by Tertiary sediments (e.g., Barito and Kutai Basins), its basement is not clear. Our results show that besides the Schwaner Block in the SW Borneo, East Borneo is also characterized by a broad, moderate strength zone of T_e=20-40 km extending from southeastern Borneo to Sarawak and Sabah (Fig. 5b). In southeastern Borneo, the Mesozoic ophiolitic and island

arc rocks of the Meratus Mountains and overlying Cretaceous turbiditic material, together with the Luk–Ulocomplex of Central Java, have been interpreted as a suture representing a destroyed Meso-Tethys ocean that separated the East Java, Bawean and Paternoster blocks from SW Borneo/Sundaland (e.g., Metcalfe, 2011). Similar rocks are exposed in West Java (e.g., Hall, 2012). Based on the outcrops of gabbroic and ultrabasic rocks on the northern margin of the Kutai Basin, and the similar initially rifting history of the Kutai and Barito basins in the Middle Eocene, Moss and Chambers (1997) suggested that the basement in East Borneo might consist of similar rocks to the Meratus Complex. Therefore, the same strength features (Fig. 5b)might indicate that East Borneo has a similar crustal basement, and represents a broad tectonic zone of the destroyed Meso-Tethys Ocean extending from West-Middle Java, through East Borneo to northern Borneo of Sarawak and Sabah. Its tectonic implication might be significant for SE Asia, and is worthy of further studies.

Since the Sunda Shelf is covered by sediment and water, the southern extension of the Indosinian zones between Indochina and Sibumasu beyond the Malay Peninsula (Metcalfe, 2011), is less touched. The recovered T_e (Figs 4b and 5b) and the subsurface load fraction (F) patterns (Fig. 10) show that the shelf region extending from offshore of the southeastern Malay peninsula to the southern coast of Borneo (the region bounded by dotted, thin, orange curves enclosing question marks in Fig. 1) shares not only the similar weak zone feature, but also the high load fraction with the onshore Indosinian zones. The region agrees well with the proposed southern extension of the Indosinian zone by Metcalfe (2011) in the Sunda shelf, but extends further eastward. Therefore, it might be reasonable to suppose that the Indosinian zones extend further southeastwards across Billiton Island to offshore of southern Borneo up to a point where they are bounded by the West-Middle Java-East Borneo tectonic zone (Figs 1, 4b and 5b).

The Singapore platform is the strongest region of the Sunda shelf. T_e features in the platform are very similar to SW Borneo. Just to the north of the Singapore platform and SW Borneo, there is a weak zone along the Lupar Line extending from the coast of western Sarawak towards Natuna Ridge. The Lupar line is thought to be a significant suture zone between the Luconia block and west Borneo (e.g., Hutchison, 1996; Fyhn et al., 2009). If the suture zone really extends from the onshore Lupar line to the Natuna Ridge, the Singapore platform and SW Borneo, which share the similar strength features and lie just to the south of the suture zone, might belong to the same block.

5.3. T_e, strain, and seismicity

The magnitude and spatial variations of T_e could control the degree, style and localization of deformation in response to long-term tectonic loads, and potentially the distribution of seismic activity (e.g., Lowry and Smith, 1995; Tassara et al., 2007; Audet and Bürgmann, 2011; Chen et al., 2013). Generally, weak regions with low T_e, especially those close to active margins, are more readily deformed than stronger regions. Though SE Asia is bounded by active convergence margins, its interior, particularly the Sunda Shelf and the Thai–Malay peninsula and Borneo, is largely free of seismicity and volcanism (Hall and Morley, 2004). Consequently, Sundaland is often described as a shield or craton. However, our results show that except for several isolated subregions with moderate or high T_e, low T_e prevails in the weak deformed core of Sundaland, as also suggested by Simons et al. (2007) (Fig. 5b). This is clearly different from T_e values in cratonic regions which are commonly associated with high T_e (> 60 km, Ebinger et al. 1989). Geodetic data show that GPS velocity decreases rapidly in active margins and adjacent regions (Simons et al., 2007). Since these adjacent regions are generally characterized by low T_e, the GPS velocity variations suggest that the displacement caused by the boundary tectonic forces has been greatly absorbed and decreased by subduction, folding and thrusting, and strike-slip faulting in the active margins and adjacent weak regions (Figs. 4b and5b). As a result, the GPS velocity of the interior regions is much lower than the bounding active margins, and the interior of SE Asia is largely free of seismicity and volcanism.

Seismicity is very intensive along the active margins (Fig.1), but differs from place to place. For example, the Sumatra fore-arc is characterized by a vast record of great historic earthquakes like those of 1797 (M8.4), 1861 (M8.5), 2004 (M9.3), 2005 (M8.6), 2007 (M8.4) (e.g., Grevemeyer and Tiwari, 2006; http://earthquake.usgs.gov/regional/neic), while the Java fore-arc is so far less seismically disturbed. Our results show that, besides in strike-slip faults and the folding-thrusting faults due to collision, high magnitude earthquakes preferentially occur in areas of steep strength variation, already observed in previous studies (e.g., Chen et al., 2013; Jiménez-Díaz et al., 2014). Since the fashion of deformation is different for materials with different strength, discontinuous deformations (such as faulting), and therefore earthquakes, are prone to occur in areas of steep strength variation where strength difference is drastic. An interesting observation is that the large rapid slip region of the Sumatra-Andaman earthquake that occurred at December 2004 (M = 9.3)

(Shapiro et al., 2008) is characterized by high T_e values. Since the regions with a large T_e gradient can be found both in the Java Margin and in the Sumatra Margin, the differing seismicity may be attributed to oblique plate convergence in the Sumatra margin. Oblique subduction led to the creation and lateral motion of the two strike-slip faults in the Sumatra margin, known as Sumatra and Mentawai fault segments, and hence occurrences of great earthquakes (Grevemeyer and Tiwari, 2006).

5.4. Loading structure

Fig. 10 displays the internal load fraction (F) values at the coherence transition wavenumber corresponding to the best fitting T_e (Figs. 4b and 5b). Although these results are based upon the outcomes of the load deconvolution and thin plate flexure models, they show intriguing correlations with seismic data in some regions of the study area.

In general, surface loading ($F< 0.5$) dominates in oceanic lithosphere (at seafloor depths >3000 m, approximately; cf. Fig. 1) which has been noted before (e.g. Watts, 2001), while the continents (and continental shelves) generally exhibit mixed ($F \sim 0.5$) or subsurface-dominated ($F> 0.5$) loading.

Subsurface loading ($F> 0.5$) dominates in the Indosinian suture zones and the relative Granite Belt extending from the Red River fault zone to the Malay Peninsula. It is also high in the coastal regions of South China, the northern margin of the South China Sea, and the coastal areas of Vietnam, which, in general, agrees with the distributions of a high-velocity lower crustal (HVLC) layer and Late Cenozoic basaltic rocks. By analyzing the deep crustal structure through the continental margins of the South China Sea, Xia et al. (2014) concluded that the HVLC layeris well developed in the eastern part of its northern margin (profiles of O1, E2, O3, O9; Fig. 11), while in the western slope area and the Xisha Trough, the HVLC layer seems unlikely to have been widely developed (profiles of O2, O4, O7; Fig. 11). An exception is found in the results of Nissen et al. (1995). They suggested that there was a very thin HVLC layer in the Xisha Trough (Profile E1 in Fig. 11). This feature of the HVLC layer distribution is consistent with the observed subsurface loading pattern (Fig. 10). Fig. 10 shows that except for the Leiqiong area (Leizhou Peninsula and the northern Hainan Island) and adjacent areas, subsurface loading dominates in the eastern part of the northern margin. The Leiqiong area is where the Hainan Hotspot lies, with associated widespread

basaltic magmatism since Pliocene (Fig. 11) (e.g., Wang et al., 2013). Seismic tomography studies also find that there is a low-*Vs* anomaly zone beneath the Hainan Hotspot (Lei et al., 2009). After analyzing their deep seismic data, Zhu Junjiang (2016, personal communication) suggests that the HVLC layer developed in the east of the Leiqiong area (Profile L1 in Fig. 11). In fact, the synchronous late Cenozoic basalts also occurred in the southwest (Penghu) of Taiwan, the deep-water area of the eastern Qiongdongnan Basin, the lower slopes of the northern margin of the South China Sea, and Indochina (Fig. 11).

The widespread Indochina Basalt plateaus in Vietnam, Thailand, Laos, and Cambodia occupy ca. 70,000 km^2 (Hoàng et al., 2013) which are located where subsurface loading dominates (Figs. 10, 11). Based on their seismic tomography data, Yang et al. (2015) also found a low-*Vs* anomaly below depths of 100 km at the coast of Indochina. The difference in the HVLC layer distribution between the eastern and western parts of the northern margin of the South China Sea might be related to the breakup of the South China Sea, which initially broke up in the east, then propagated westward (Sun et al., 2009). After the cessation of seafloor spreading at 16 Ma, basaltic magmatism due to deep thermal anomalies became active in the South China Sea and adjacent regions. The magmatism fed by the deep low-velocity anomaly source might not only have developed the surface basalt, but also given rise to the subsurface loads shown in Fig. 10.

6. Conclusions

We have generated high-resolution maps of the spatial variations of T_e for SE Asia using the wavelet method, by eliminating the effect of less dense sediments on the recovered T_e values. We find that the sediment-corrected T_e maps correlate better with the geology, particularly in elongated rift basins where very thick sediments have been deposited, and also with the results of previous studies. The sediment-uncorrected results are much higher than expected, suggesting that the thick sediment has a detrimental effect on T_e modeling. The pattern of the T_e variations in SE Asia, in general, agrees well with the tectonic provinces and related major tectonic boundaries. The oceanic basins, the Indosinian suture zones between the Indochina and Sibumasu blocks, and the Makassar Strait are characterized by low T_e. Moderate and high T_e values occur in the Khorat plateau, West Burma, the Singapore Ridge, the Con Song Swell, Borneo, the northern Australian margin and the Molucca Sea. The Khorat plateau has the strongest lithosphere in the Indochina Block. The strength

of the Indonesian margin shows a relatively complex pattern. In general, the incoming oceanic plate becomes weaker when approaching the trench axis. However, the T_e pattern in the subduction system, particularly in the southern Sumatra Trench and Java trench is complicated by the approach and collision of oceanic plateaus and seamounts with the fore-arc region.

Our results show that the Indochina Peninsula is heterogeneous in rheological strength, and that strong, central Indochina is surrounded by broad and linear weak zones. Although the western Indochina Peninsula has been extruded southeastwards several hundred kilometers during the India-Eurasia collision, the displacement might have been partitioned and absorbed by the combined mechanism of the extrusion and viscous tectonic models. As a result, the offshore displacements of the major strike-slip faults in the South China Sea are much smaller than originally assumed, thus having had less effect on the development of the South China Sea than other mechanisms such as the slab pull of the proto-South China Sea.

Our results show that besides the Schwaner Block in SW Borneo, East Borneo is also characterized by a broad moderate strength zone of T_e=20-40 km extending from southeastern Borneo into Sarawak and Sabah. Together with other geological evidence, this strength feature might indicate that East Borneo has a similar crustal basement, and represents a broad tectonic zone of the destroyed Meso-Tethys Ocean extending from West-Middle Java, through East Borneo to northern Borneo of Sarawak and Sabah. Our results suggest that the Indosinian zones between the Indochina and Sibumasu blocks extend further southeastward across Billiton Island to offshore of the southern part of Borneo, and that the Singapore platform and SW Borneo, which share similar strength features and lie just to the south of the Lupar suture zone, might belong to the same block.

Our results show that several isolated subregions with moderate or high T_e are bounded by low T_e regions in the weak deformed core of Sundaland as suggested by Simons et al. (2007). The displacement caused by the boundary tectonic forceshasbeen greatly absorbed and decreased by subduction and deformation in the marginal regions and adjacent weak regions. As a result, the velocity of the interior regions is greatly lower than the active boundary margins, and these regions are largely free of seismicity and volcanism.

The results show that the internal load fraction F is high in the coastal area of South China, the northern margin of the South China Sea, and the coastal area of Indochina, which, in general, agrees with the distributions of a high-velocity lower crustal layer and Late Cenozoic basaltic rocks.

The difference of the HVLC layer distribution between the east and west of the northern margin of the South China Sea might be related to the breakup of the South China Sea. Subsurface loading (higher density materials) dominates in the eastern lowermost crust where the South China Sea initially broke up. The basaltic magmatism in the Late Cenozoic might not only develop the surface basalt, but also form the subsurface loads.

Acknowledgements

We are grateful to two anonymous reviewers for their constructive and valuable comments that helped to greatly improve the quality of the manuscript. We would like to thank Chris Swain for his kind guidance in data processing and interpretation, and Robert Hall for making valuable comments on our earlier results. All figures, except for Fig. 9, were plotted using GMT (Wessel et al., 2013; available at http://gmt.soest.hawaii.edu/home). This work was jointly supported by the National Natural Science Foundation of China (Grant 41376059, 41576036, 41176050).

References

Addison, P.S., Watson, J.N., Feng, T., 2002. Low-oscillation complex wavelets, Journal of Sound and Vibration 254(4): 733-762.

Audet, P., Bürgmann, R., 2011. Dominant role of tectonic inheritance in supercontinent cycles. Nat. Geosci. 4, 184–187.

Bassin, C., Laske, C., Masters, T.G., 2000. The current limits of resolution for surface wave tomography in North America, Eos Trans. AGU, 81(48), Fall Meet Suppl., Abstract S12A-03.

Braitenberg, C., Wienecke, S., Wang, Y., 2006. Basement structures from satellite-derived gravity field: South China Sea ridge. Journal of Geophysical Research, 111, doi:10.1029/2005jb003938.

Briais, A., Patriat, P., Tapponnier, P., 1993. Updated interpretation of magnetic anomalies and seafloor spreading stages in the South China Sea: implications for the tertiary tectonics of Southeast Asia. J. Geophys. Res. 98 (B4), 6299–6328.

British Oceanographic Data Centre, 2008. The Centenary Edition of theGEBCO Digital Atlas, http://www.gebco.net.

Bry, M., White, N., 2007.Reappraising elastic thickness variation at oceanic trenches. Journal of Geophysical Research 112, B08414, doi:08410.01029/02005JB004190.

Burov, E.B., 2011. Rheology and strength of the lithosphere. Marine and Petroleum Geology 28, 1402-1443.

Burov, E.B., Diament, M., 1995.The effective elastic thickness of (Te) continental lithosphere. What does it really means?. J. Geophys. Res. 100 (B3), 3905–3927.

Chen, B., Chen, C., Kaban, M.K., Du, J., Liang, Q., Thomas, M., 2013. Variations of the effective elastic thickness over China and surroundings and their relation to the lithosphere dynamics. Earth Planet. Sci. Lett. 363, 61–72.

Clift, P., Lin, J., Barckhausen, U., 2002. Evidence of low flexural rigidity and low viscosity lower continental crust during continental break-up in the South China Sea.Marine and Petroleum Geology 19, 951– 970.

Cullen, A., 2014. Nature and significance of the West Baram and Tinjar Lines, NW Borneo.Marine and Petroleum Geology. 51, 197-209.

Ebinger, C.J., Bechtel, T.D., Forsyth, D.W., Bowin, C.O., 1989.Effective elastic thickness beneath the East African and Afar plateaus and dynamic compensation for the uplifts. J. Geophys. Res. 94, 2883–2901.

England, P., Houseman, G., 1986. Finite strain calculations of continental deformation 2. Comparison with the India-Asia collision zone. J. Geophys. Res. 91, 3664–3676.

Forsyth, D.W., 1985. Subsurface loading estimates of the flexural rigidity of continental lithosphere. J. Geophys. Res. 90, 12,623–12,632.

Fullea, J., Fernàndez, M., Zeyen, H., 2008. FA2BOUG – A FORTRAN 90 code to compute Bouguer gravity anomalies from gridded free air anomalies: application to the Atlantic–Mediterranean transition zone. Comput. Geosci. 34, 1665–1681.

Fyhn, M.B., Boldreel, L.O., Nielsen, L.H., 2009. Geological development of the Central and South Vietnamese margin: implications for the establishment of the South China Sea, Indochinese escape tectonics and Cenozoic volcanism. Tectonophysics 478, 184–214.

Grevemeyer, I., Tiwari, V., 2006. Overriding plate controls spatial distribution of megathrust earthquakes in the Sunda–Andaman subduction zone. Earth and Planetary Science Letters 251, 199-208.

Hall, R., 2012. Late Jurassic–Cenozoic reconstructions of the Indonesian region and the Indian Ocean. Tectonophysics 570-571, 1-41.

Hall, R., Cloke, I.R., Nur'aini, S., Puspita, S.D., Calvert, S.J., Elders, C.F., 2009. The North Makassar Straits: what lies beneath? Petroleum Geoscience 15, 147-158.

Hall, R., Morley, C.K., 2004. Sundaland Basins. In: Clift, P., Wang, P., Kuhnt, W., Hayes, D.E. (Eds.), Continent–Ocean Interactions within the East Asian Marginal Seas. Geophysical Monograph, 149. American Geophysical Union, Washington, D.C., pp. 55–85.

Hall, R., Spakman, W., 2015. Mantle structure and tectonic history of SE Asia. Tectonophysics 658, 14-45.

Hall, R., van Hattum, M.W.A., Spakman, W., 2008. Impact of India–Asia collision on SE Asia: The record in Borneo. Tectonophysics 451, 366-389.

Hilde, T.W.C., Lee, C.-S., 1984. Origin and evolution of the West Philippine Basin: a new interpretation. Tectonophysics 102, 85–104.

Hinschberger, F., Malod, J.-A., Rehault, J.-P., Villeneuve, M., Royer, J.-Y., Burhanuddin, S., 2005. Late Cenozoic geodynamic evolution of eastern Indonesia. Tectonophysics 404, 91–118.

Hoàng, N., Flower, M.F.J., Chí, C.T.ọ.n., Xuân, P.T., Quý, H.V., Sơn, T.T., 2013. Collision-induced basalt eruptions at Pleiku and BuônMêThuột, south-central Viet Nam. Journal of Geodynamics 69, 65-83.

Huang, Z., Zhao, D., Wang, L., 2015. P wave tomography and anisotropy beneath Southeast Asia: Insight into mantle dynamics, J. Geophys. Res. Solid Earth, 120, 5154–5174, doi:10.1002/2015JB012098.

Hutchison, C.S., 1996. The ‘Rajang accretionary prism’ and ‘Lupar Line’ problem of Borneo. In: Hall, R., Blundell, D.J. (Eds.), Tectonic Evolution of Southeast Asia. Geological Society of London Special Publication, pp. 247–261, 106.

Ishizuka, O., Taylor, R.N., Ohara, Y., Yuasa, M., 2013. Upwelling, rifting, and age-progressive magmatism from the Oki-Daito mantle plume. Geology 41, 1011-1014.

Jiménez-Díaz, A., Ruiz, J., Pérez-Gussinyé, M., Kirby, J.F., Álvarez-Gómez, J.A., Tejero, R., Capote, R., 2014. Spatial variations of effective elastic thickness of the lithosphere in Central America and surrounding regions. Earth Planet. Sci. Lett. 391, 55–66.

Karner, G.D., Watts, A.B., 1983. Gravity anomalies and flexure of the lithosphere at mountain

ranges. Journal of Geophysical Research 88(B12), 10,449-10,477.

Kirby, J.F., 2005. Which wavelet best reproduces the Fourier power spectrum? Computers and Geosciences, 31(7), 846-864.

Kirby, J.F., 2014. Estimation of the effective elastic thickness of the lithosphere using inverse spectral methods: The state of the art. Tectonophysics 631, 87-116.

Kirby, J.F., Swain, C.J., 2004. Global and local isostatic coherence from the wavelet transform, *Geophysical Research Letters*, **31**(24): L24608, doi:10.1029/2004GL021569.

Kirby, J.F., Swain, C.J., 2008. An accuracy assessment of the fan wavelet coherence method for elastic thickness estimation. Geochem.Geophys.Geosyst., 9, Q03022, doi:10.1029/2007GC001773.

Kirby, J.F., Swain, C.J., 2009. A reassessment of spectral T_e estimation in continental interiors: the case of North America. Journal of Geophysical Research**114**(B8), B08401, doi:10.1029/2009JB006356.

Kirby, J.F., Swain, C.J., 2011. Improving the spatial resolution of effective elastic thickness estimation with the fan wavelet transform. Comput.Geosci. 37, 1345–1354.

Kirby, J.F., Swain, C.J., 2013. Power spectral estimates using two-dimensional Morlet-fan wavelets with emphasis on the long wavelengths: jackknife errors, bandwidth resolution and orthogonality properties. Geophysical Journal International **194,** 78-99.

Lacassin, R., Replumaz, A., Leloup, P.H., 1998. Hairpin river loops and slip-sense inversion on southeast Asian strike-slip faults, Geology, 26(8), 703–706.

Lei, J., Zhao, D., Steinberger, B., Wu, B.,Shen, F., Li,Z., 2009.New seismic constraints on the upper mantle structure of the Hainan plume. Phys. Earth Planet. Inter. 173, 33–50.

Lester, R., Van Avendonk, H.J.A., McIntosh, K., Lavier, L., Liu, C.S., Wang, T.K., Wu, F., 2014. Rifting and magmatism in the northeastern South China Sea from wide-angle tomography and seismic reflection imaging. Journal of Geophysical Research: Solid Earth 119, 2305-2323.

Li, C.F., Xu, X., Lin, J., Sun, Z., Zhu, J., Yao, Y.J., Zhao, X.X., Liu, Q.S., Kulhanek, D.K., Wang, J., Song, T.R., Zhao, J.F., Qiu, N., Guan, Y.X., Zhou, Z.Y., Williams, T., Bao, R., Briais, A., Brown, E.A., Chen, Y.F., Clift, P.D., Colwell, F.S., Dadd, K.A., Ding, W.W., Almeida, I.H., Huang, X.L., Hyun, S.M., Jiang, T., Koppers, A.A.P., Li, Q.Y., Liu, C.L., Liu, Z.F., Nagai, R.H., Peleo-Alampay, A., Su, X., Tejada, M.L.G., Trinh, H.S., Yeh, Y.C., Zhang, C.L., Zhang, F.,

Zhang, G.L., 2014. Ages and magnetic structures of the South China Sea constrained by deep tow magnetic surveys and IODP Expedition 349. Geochemistry Geophysics Geosystems 15, 4958-4983.

Li, C., Van der Hilst, R.D., Toksöz, M.N., 2006. Constraining P‐wave velocity variations in the upper mantle beneath Southeast Asia, Phys. Earth Planet.Inter., 154, 180–195, doi:10.1016/j.pepi.2005.09.008.

Lin, A., Watts, A., 2002. Origin of the west Taiwan basin by orogenic loading and flexure of a rifted continental margin. Journal of Geophysical Research 107 (B9), 2185.doi: 10.1029/ 2001JB000669.

Lin, A.T., Watts, A.B., Hesselbo, S.P., 2003. Cenozoic stratigraphy and subsidence history of the South China Sea margin in the Taiwan region. Basin Res. 15, 453-478, doi:10.1046/j.1365-2117.2003.00215.x.

Lowry, A.R., Smith, R.B., 1994. Flexural rigidity of the Basin and Range-Colorado Plateau-Rocky Mountain transition from coherence analysis of gravity and topography. Journal of Geophysical Research 99(B10), 20,123-20,140.

Lowry, A.R., Smith, R.B., 1995. Strength and rheology of the western U.S. Cordillera. J. Geophys. Res. 100, 17,947–17,963.

Madon, M.B., Watts, A.B., 1998. Gravity anomalies, subsidence history and the tectonic evolution of the Malay and Penyu basins (offshore Peninsular Malaysia). Basin Research 10, 375–392.

Mao, X.,Wang, Q., Liu, S., Xu,M.,Wang, L., 2012. Effective elastic thickness andmechanical anisotropy of South China and surrounding regions. Tectonophysics 550–553, 47–56.

McKenzie, D., 2003. Estimating Te in the presence of internal loads. Journal of Geophysical Research 108 (B9), 2438.doi:10.1029/2002JB001766.

McKenzie, D., Fairhead, J.D., 1997. Estimates of the effective elastic thickness of the continental lithosphere from Bouguer and free air gravity anomalies. J. Geophys. Res. 102 (B12), 27,523–27,552.

Metcalfe, I., 2011. Tectonic framework and Phanerozoic evolution of Sundaland. Gondwana Research 19, 3–21.

Morley, C.K., 2012. Late Cretaceous–Early Palaeogene tectonic development of SE Asia. Earth-Science Reviews 115, 37-75.

Morley, C.K., 2013. Discussion of tectonic models for Cenozoic strike-slip fault-affected continental margins of mainland SE Asia. J. Asian Earth Sci. 76, 137–151.

Moss, S.J., Chambers, J.L.C., 1999. Tertiary facies architecture in the Kutai Basin. Tectonics, Stratigraphy and Petroleum Systems of Borneo Workshop, Brunei 1997 Spec. Ed. J. Asian Earth Sci. 17, 157-181.

Mouthereau F., Petit C., 2003. Rheology and strength of the Eurasian continental lithosphere in the foreland of the Taiwan collision belt: Constraints from seismicity, flexure, and structural styles. J. Geophys. Res. 108 (B11), 2512, doi:10.1029/2002JB002098.

Nair RR.,Maji TK., Maiti T. et al., 2011. Multitaper coherence method for appraising the elastic thickness of the Indonesian active continental margin. Journal of Asian Earth Sciences 40: 326-333.

Nissen, S.S., Hayes, D.E., Buhl, P., Diebold, J., Yao, B.C., Zeng, W.J., Chen, Y.Q., 1995. Deep penetration seismic soundings across the northern margin of the South China Sea. Journal of Geophysical Research 100 (B11), 22407–22433.

Ozawa, A., Tagami, T., Listanco, E.L., Arpa, C.B., Sudo, M., 2004. Initiation and propagation of subduction along the Philippine Trench: Evidence from the temporal and spatial distribution of volcanoes, J. Asian Earth Sci., 23, 105–111.

Pavlis, N.K., Holmes, S.A., Kenyon,S.C., Factor, J.K., 2012. The development and evaluation of the Earth Gravitational Model 2008 (EGM2008), *Journal of Geophysical Research* 117, B04406, doi:10.1029/2011JB008916.

Pérez-Gussinyé, M., Lowry, A.R., Watts, A.B., 2007. Effective elastic thickness of South America and its implications for intracontinental deformation. Geochem. Geophys. Geosyst. 8, Q05009, doi:10.1029/2006GC001511.

Pérez-Gussinyé, M., Lowry, A.R., Morgan, J.P., Tassara, A., 2008. Effective elastic thickness variations along the Andean margin and their relationship to subduction geometry. Geochem.Geophys. Geosyst. 9, Q02003.

Pérez-Gussinyé, M., Swain, C.J., Kirby, J.F., Lowry, A.R., 2009. Spatial variations of the effective elastic thickness, T_e, using multitaper spectral estimation and wavelet methods: examples from synthetic data and application to South America. Geochemistry, Geophysics, Geosystems

10(4), Q04005, doi:10.1029/2008GC002229.

Press, W.H., Teukolsky, S.A., Vetterling, W.T., Flannery, B.P., 1992. Numerical Recipes in Fortran 77, 2nd Ed., Cambridge University Press, Cambridge.

Pubellier, M., Monnier, C., Ali, J., 2003. Cenozoic plate interaction of the Australia and Philippine Sea plates: hit-and-run tectonics. Tectonophysics 363, 181-199.

Ranalli, G., 1997. Rheology of the lithosphere in space and time. Geol. Soc. (Lond.) Spec. Publ. 121, 19–37.

Rao, D.B., Babu, D.N., 1991. A Fortran-77 computer program for three dimensional analysis of gravity anomalies with variable density contrast. Computers and Geosciences 17 (5), 655–667.

Ratheesh-Kumar, R.T., Maji, T.K., Nair, R.R., 2010.Assessment of flexural analysis applied to the Sumatra–Java subduction zone. Journal of Earth System Sciences 119 (5), 717–730.

Searle, M.P., Morley, C.K., 2011. Tectonic and thermal evolution of Thailand in the regional context of SE Asia. In: Ridd, M.F., Barber, A.J., Crow, M.J. (Eds.), The Geology of Thailand, Geological Society of London, Memoir, pp. 539–571(Chapter 20).

Shapiro, N.M., Ritzwoller, M.H., Engdahl, E.R., 2008. Structural context of the great Sumatra-Andaman Islands earthquake, Geophysical Research Letters 35, L05301, doi:10.1029/2008GL033381.

Shi, X., Qiu, X., Xia, K., Zhou, D., 2003. Characteristics of surface heat flow in the South China Sea. J. Asian Earth Sci., 22, 265–277.

Shi, X., Burov, E., Leroy, S., et al., 2005. Intrusion and its implication for subsidence: a case from the Baiyun Sag, on the Northern Margin of the South China Sea. Tectonophysics 407(1-2), 117-134.

Singsoupho, S., Bhongsuwan, T., Elming, S.-Å., 2014. Tectonic evaluation of the Indochina Block during Jurassic-Cretaceous from palaeomagnetic results of Mesozoic redbeds in central and southern Lao PDR. Journal of Asian Earth Sciences 92, 18-35.

Simons WJF.,Socquet A., Vigny C., et al., 2007. A decade of GPS in Southeast Asia: Resolving Sundaland motion and boundaries. Journal of Geophysical Research 112, B06420, doi:10.029/2005JB003868.

Stark, C.P., Stewart, J., Ebinger, C.J., 2003. Wavelet transform mapping of effective elastic thickness and plate loading: Validation using synthetic data and application to the study of

southern African tectonics. Journal of Geophysical Research 108, 2558.

Su D., 2012. A study of the effective elastic thickness of the Oceanic lithosphere. Chinese Journal of Geophysics, 55(10), 3259-3265.

Sun, Z., Zhong, Z.H., Keep, M., Zhou, D., Cai, D.S., Li, X.S., Wu, S.M., Jiang, J.Q., 2009. 3D analogue modeling of the South China Sea: a discussion on breakup pattern. J. Asian Earth Sci. 34 (4), 544–556. http://dx.doi.org/10.1016/j.jseaes.2008.09.002.

Swain, C.J., Kirby, J.F., 2003.The effect of 'noise' on estimates of the elastic thickness of the continental lithosphere by the coherence method. Geophys. Res. Lett. 30(11): 1574, doi:10.1029/2003GL017070.

Swain, C.J., Kirby, J.F., 2006. An effective elastic thickness map of Australia from wavelet transforms of gravity and topography using Forsyth's method. Geophys. Res. Lett. 33, L02314.http://dx.doi.org/10.1029/2005GL025090.

Takemoto, K., Sato, S., Chanthavichith, K., Inthavong, T., Inokuchi, H., Fujihara, M., Zaman, H., Yang, Z., Yokoyama, M., Iwamoto, H., Otofuji, Y.-i., 2009. Tectonic deformation of the Indochina Peninsula recorded in the Mesozoic palaeomagnetic results. Geophysical Journal International 179, 97-111.

Tang,Q., Zheng, C., 2013. Crust and upper mantle structure and its tectonic implications in the South China Sea and adjacent regions. J. Asian Earth Sci. 62, 510–525.

Tapponnier, P., Peltzer, G., Le Dain, A.Y., Armijo, R., Cobbold, P., 1982. Propagating extrusion tectonics in Asia: new insights from simple experiments with plasticine. Geol. 10, 611–616.

Tassara, A., Swain, C., Hackney, R., Kirby, J., 2007. Elastic thickness structure of South America estimated using wavelets and satellite-derived gravity data. Earth and Planetary Science Letters 253, 17-36.

Taylor, B., Hayes, D.E., 1983. Origin and history of the South China Sea Basin. In: D. E.Hayes (Editor). The Tectonic and Geologic Evolution of Southeast Asian Seas and Islands, 2. Am. Geophys. Union Geophys.Monogr., 27:23-56.

Tran, H.T., Zaw, K., Halpin, J., Manaka, T., Meffre, S., Lai, C.K., Lee, Y.J., Le, V.H., Dinh, S., 2014.The Tam Ky–Phuoc Son shear zone in Central Vietnam: tectonic and metallogenic implications. Gondwana Research, http://dx.doi.org/10.1016/j.gr.2013.04.008.

Wang, X.C., Li, Z.X., Li, X.H., Li, J., Xu, Y.G., Li, X.H., 2013. Identification of an ancient mantle

reservoir and young recycled materials in the source region of a young mantle plume: Implications for potential linkages between plume and plate tectonics. Earth and Planetary Science Letters 377-378, 248-259.

Wang, Y., Sieh, K., Tun, S.T., Lai, K.Y., Myint, T., 2014. Active tectonics and earthquake potential of the Myanmar region, J. Geophys. Res. Solid Earth, 119, 3767–3822, doi:10.1002/2013JB010762.

Watts, A.B., 2001. Isostasy and Flexure of the Lithosphere. Cambridge University Press. 472 pp.

Wessel, P., Smith, W.H.F., Scharroo, R., Luis, J.F., Wobbe, F., 2013. Generic mapping tools: Improved version released. Eos Trans. AGU 94, 409–410.

Whittaker, J., Goncharov, A., Williams, S., Müller, R.D., Leitchenkov, G., 2013. Global sediment thickness dataset updated for the Australian-Antarctic Southern Ocean. Geochem. Geophys. Geosyst. 14 (8), 2547-3313. DOI: 10.1002/ggge. 20181.

Xia S., Guo X., Huang H., Qiu X., 2014. Geophysical features of lithosphere and tectonic boundaries in the South China Sea. Chinese Journal of Geophysics, 57(12):3957-3967.

Yang, T., Liu, F., Harmon, N., Le, K.P., Gu, S., Xue, M., 2015. Lithospheric structure beneath Indochina block from Rayleigh wave phase velocity tomography. Geophysical Journal International 200, 1582-1595.

Yu C., Shi X., Tang Q., Yang X., 2017. The thermal lithosphere thickness of the Southeast Asia. Marine Geophysical Research, submitted.

Table and Figure Captions

Table 1. Symbols and values of constants

Fig. 1. Tectonic outline and topography/bathymetry in and around SE Asia. The purple and pink regions denote the Indosinian suture zones and the relative Permian and Triassic Granite Belt between the Indochina Block and the Sibumasu Block, respectively. From north to south, the former comprises the Changning–Menglian suture in southwest China, the Inthanon suture in Thailand, and the Bentong-Raub suture in the Malay Peninsula, the latter comprises the Lincang Granitoid

Batholith in China, Sukhothai in Thailand, and East Malaya in the Malay Peninsula) in the east (Metcalfe, 2011). The region with question marks encompassed by the thin, dotted orange thin curves denotes the supposed southeastward extension of the Indosinian suture zones and the Granite Belt. The region encompassed by the thick, dashed, deep red curve is the undeformed core of SE Asia suggested by Simons et al. (2007). Red arrows denote the approximate (absolute/ITRF2000) motions of different plates (after Simons et al., 2007). The red triangles denote Holocene volcanoes from the Global Volcanism Program. Abbreviations: AS, Andaman Sea; BB, Barito Basin; BI, Billiton Island; CCS, Con Song Swell; CS, Celebes Sea; EJWS, East Java-West Sulawesi Block; ELT, East Luzon Trough;HA, HalmaheraArc; HN, Hainan Island; KB, Kutai Basin; KPR, Kyushu-Palau Ridge;LL, Lupar Line;LZ, Leizhou Peninsula; MAS, Makassar Strait;MB, Malay Basin; MF, Mentawai Fault; MLS, Meratus and Luk Ulo Sutures; MM, Meratus Mountains; MPF, Mae Ping Fault; MS, Molucca Sea;MT, Manila Trench; NBS, North Banda Sea; NSB, Nansha Block (Dangerous Grounds and Reed Bank); NT, Nansha Trough (NW Borneo Trough); PB, Penyu Basin; PF, Philippine Fault; PRMB, Pearl River Mouth Basin; PT, Philippine Trench; QDNB, Qiongdongnan Basin; RR, Roo Rise; RRFZ, Red River Fault Zone; SA, SangiheArc; SB, Semitau Block; SBS, South Banda Sea; SFZ, Sumatra Fault Zone;SGF, Sagaing Fault; SM, Schwaner Mountains; SR, Singapore Ridge;SS, Sulu Sea;SWB, Southwest Borneo Block; TPF, Three Pagodas Fault; TT, Timor Trough; TW, TaiwanIsland; WB, West Burma; WPS, West Philippine Sea; WS, West Sumatra Block; XS, Xisha Trough; XZB, Xisha-Zhongsha Block; YB, Yinggehai Basin.

Fig. 2. (a) The free-air and (b) complete Bouguer gravity anomalies of SE Asia.

Fig. 3. (a) Sediment thickness and (b) the relative negative gravity anomaly in SE Asia. Abbreviations: MP, Malay Peninsula; HN, Hainan Island; TW, Taiwan Island; LZ, Luzon Island.

Fig. 4.T_e estimates from $|\mathbf{k}_0|$ = 2.668in SE Asia. (a) Sediment-uncorrected;(b)sediment-corrected. The yellow dashed curve shows the ocean-continent boundary of the South China Sea. Tectonic lines are the same as for Fig. 1 (Some in different color for readability).

Fig. 5.T_e estimates from $|\mathbf{k}_0|$ = 3.773in SE Asia. (a) Sediment-uncorrected;(b)sediment-corrected. The yellow dashed curve shows the ocean-continent boundary of the South China Sea. Yellow solid points refer to earthquakes (Ms> 7.0, www.isc.ac.uk), and the great historic earthquakes in the Sunda subduction system (Sumatra and Java trenches) (Grevemeyer and Tiwari, 2006). The red quadrilateral region over the northwest of Sumatra shows the large rapid slip region of the Sumatra-Andaman earthquake that occurred in December 2004 (M = 9.3) (Shapiro et al., 2008). Tectonic lines are the same as for Fig. 1 (Some in different color for readability).

Fig. 6.Cross sections along the profile shown in Fig. 5, from south to north. (a) T_e (km); (b) observed Bouguer squared real coherency (SRC);(c) predicted Bouguer SRC. The black contour in (b) and (c) is SRC = 0.5. EFW on the ordinate in (b) and (c) is equivalent Fourier wavelength.

Fig. 7.Sediment-corrected T_e estimates in SE Asia with regions of the maximum value of the normalized free-air SIC $\overline{\Gamma}^2_{F,I} > 0.5$ masked in grey. (a) $|\mathbf{k}_0|$ = 2.668; (b) $|\mathbf{k}_0|$ = 3.773.

Fig. 8. Regional surface heat flow in SE Asia.The heat flow data in the South China Sea are collected from Shi et al. (2003) and recent contributions. The heat flow data in the adjacent area of the South China Sea are from the updated global heat flow database of the International Heat Flow Commission. To be noted, because ofthe limited heat flow data set, and their extremely uneven distribution,the heat flow map, which is drawn directly based on the data set,is not always reliable, and might be fraudulent and misleadingin the regions with few or no heat flow stations.

Fig. 9. Schematic diagrams of rigid bodies influencing local deformation. LF, Lancang strike-slip fault; MF, Mengxing strike-slip fault; RRFZ, Red River Fault Zone; WBL, West Baram Line; TL, Tinjar Line.

Fig. 10.Internal load fraction, F, corresponding to the above recovered T_e.(a) $|\mathbf{k}_0|$ = 2.668; (b) $|\mathbf{k}_0|$ = 3.773. The red triangles denote Holocene volcanoes from the Global Volcanism Program (http://volcano.si.edu/). Tectonic lines are the same as for Fig. 1 (Some in different color for

readability).

Fig.11. Crustal structure sections (O1, O2 and O3) based on deep seismic data through the continental margins of the South China Sea. Inset (a) shows the locations of these sections.

Table 1. Symbols and values of constants

Constant	Symbol	Value	Units
Young's modulus	E	100	GPa
Newtonian gravitational constant	G	6.6726×10^{-11}	$m^3\,kg^{-1}\,s^{-2}$
Poisson 's ratio	σ	0.25	
Gravity acceleration	g	9.79	$m\,s^{-2}$
Seawater density	ρ_w	1030	$kg\,m^{-3}$
Upper crust density	ρ_{uc}	2670	$kg\,m^{-3}$
Crust density	ρ_c	2800	$kg\,m^{-3}$
Mantle density	ρ_m	3300	$kg\,m^{-3}$

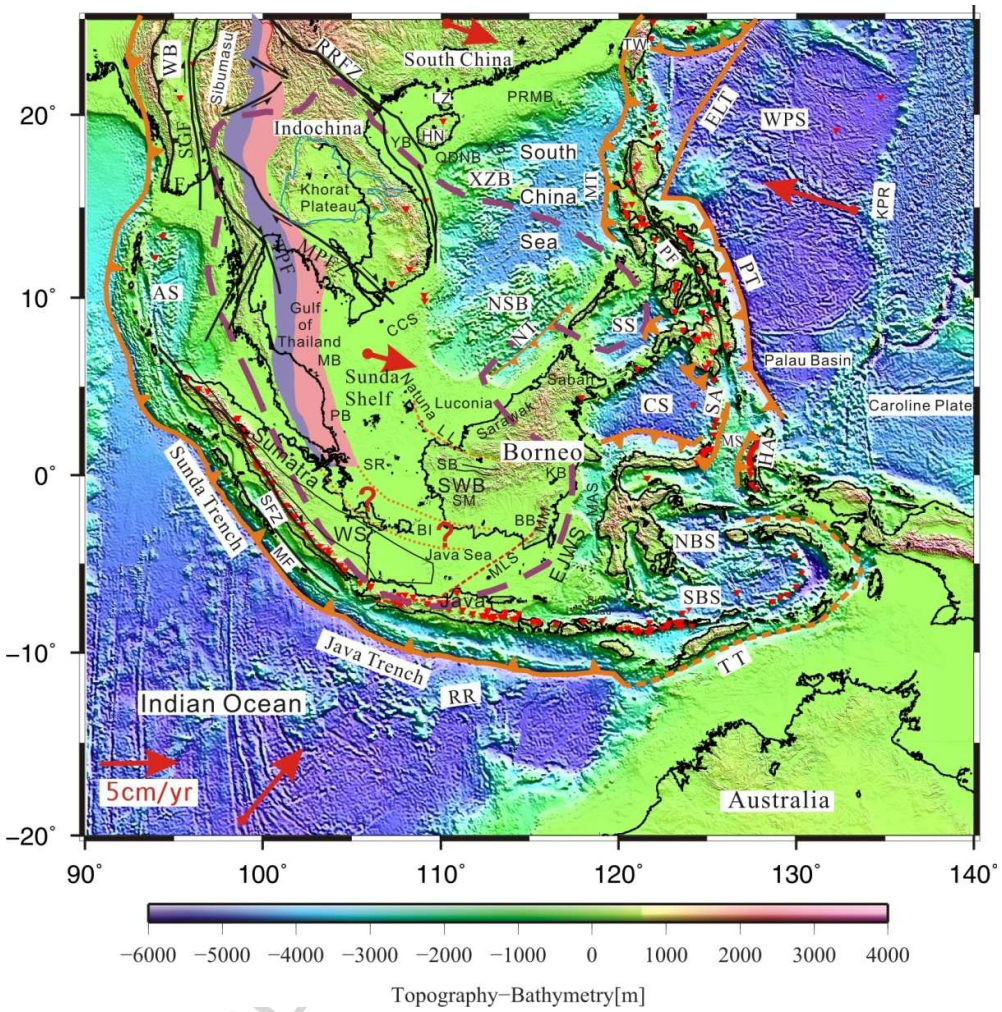

Fig. 1. Tectonic outline and topography/bathymetry in and around SE Asia. The purple and pink regions denote the Indosinian suture zones and the relative Permian and Triassic Granite Belt between the Indochina Block and the Sibumasu Block, respectively. From north to south, the former comprises the Changning–Menglian suture in southwest China, the Inthanon suture in Thailand, and the Bentong-Raub suture in the Malay Peninsula, the latter comprises the LincangGranitoid Batholith in China, Sukhothai in Thailand, and East Malaya in the Malay Peninsula) in the east (Metcalfe, 2011). The region with question marks encompassed by the thin, dotted orange thin curves denotes the supposed southeastward extension of the Indosinian suture zones and the Granite Belt. The region encompassed by the thick, dashed, deep red curve is the undeformed core of SE Asia suggested by Simons et al. (2007). Red arrows denote the approximate (absolute/ITRF2000) motions of different plates (after Simons et al., 2007). The red triangles denote Holocene volcanoes from the Global Volcanism Program. Abbreviations: AS, Andaman Sea; BB, Barito Basin; BI,

Billiton Island; CCS, Con Song Swell; CS, Celebes Sea; EJWS, East Java-West Sulawesi Block; ELT, East Luzon Trough;HA, Halmahera Arc; HN, Hainan Island; KB, Kutai Basin; KPR, Kyushu-Palau Ridge;LL, Lupar Line;LZ, LeizhouPeninsula; MAS, Makassar Strait;MB, Malay Basin; MF, Mentawai Fault; MLS, Meratus and LukUlo Sutures; MM, Meratus Mountains; MPF, Mae Ping Fault; MS, Molucca Sea;MT, Manila Trench; NBS, North Banda Sea; NSB, Nansha Block (Dangerous Grounds and Reed Bank); NT, Nansha Trough (NW Borneo Trough); PB, Penyu Basin; PF, Philippine Fault; PRMB, Pearl River Mouth Basin; PT, Philippine Trench; QDNB, Qiongdongnan Basin; RR, Roo Rise; RRFZ, Red River Fault Zone; SA, Sangihe Arc; SB, Semitau Block; SBS, South Banda Sea; SFZ, Sumatra Fault Zone;SGF, Sagaing Fault; SM, Schwaner Mountains; SR, Singapore Ridge;SS, Sulu Sea;SWB, Southwest Borneo Block; TPF, Three Pagodas Fault; TT, Timor Trough; TW, Taiwan Island; WB, West Burma; WPS, West Philippine Sea; WS, West Sumatra Block; XS, Xisha Trough; XZB, Xisha-Zhongsha Block; YB, Yinggehai Basin.

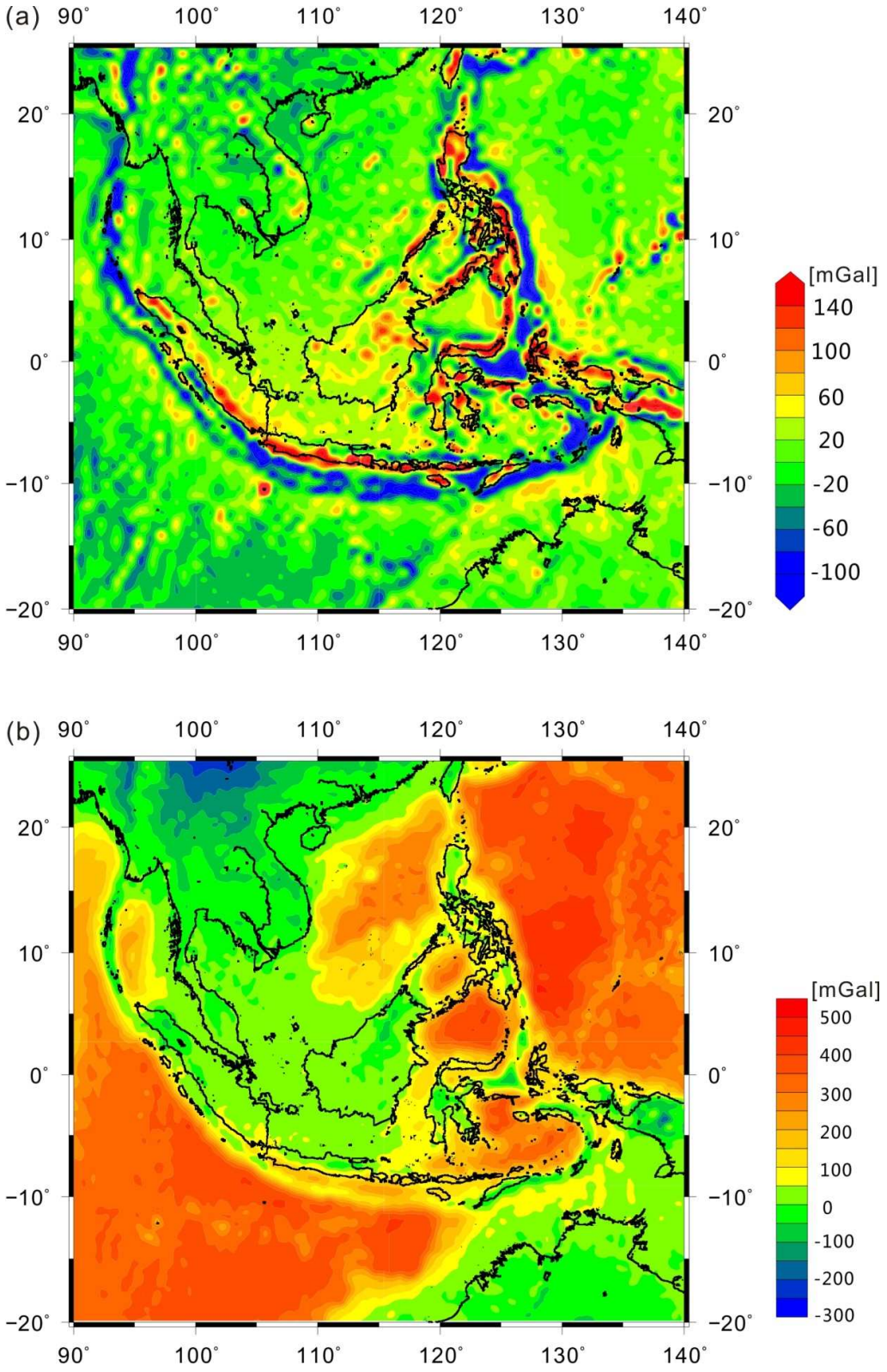

Fig. 2. (a) The free-air and (b) complete Bouguer gravity anomalies of SE Asia.

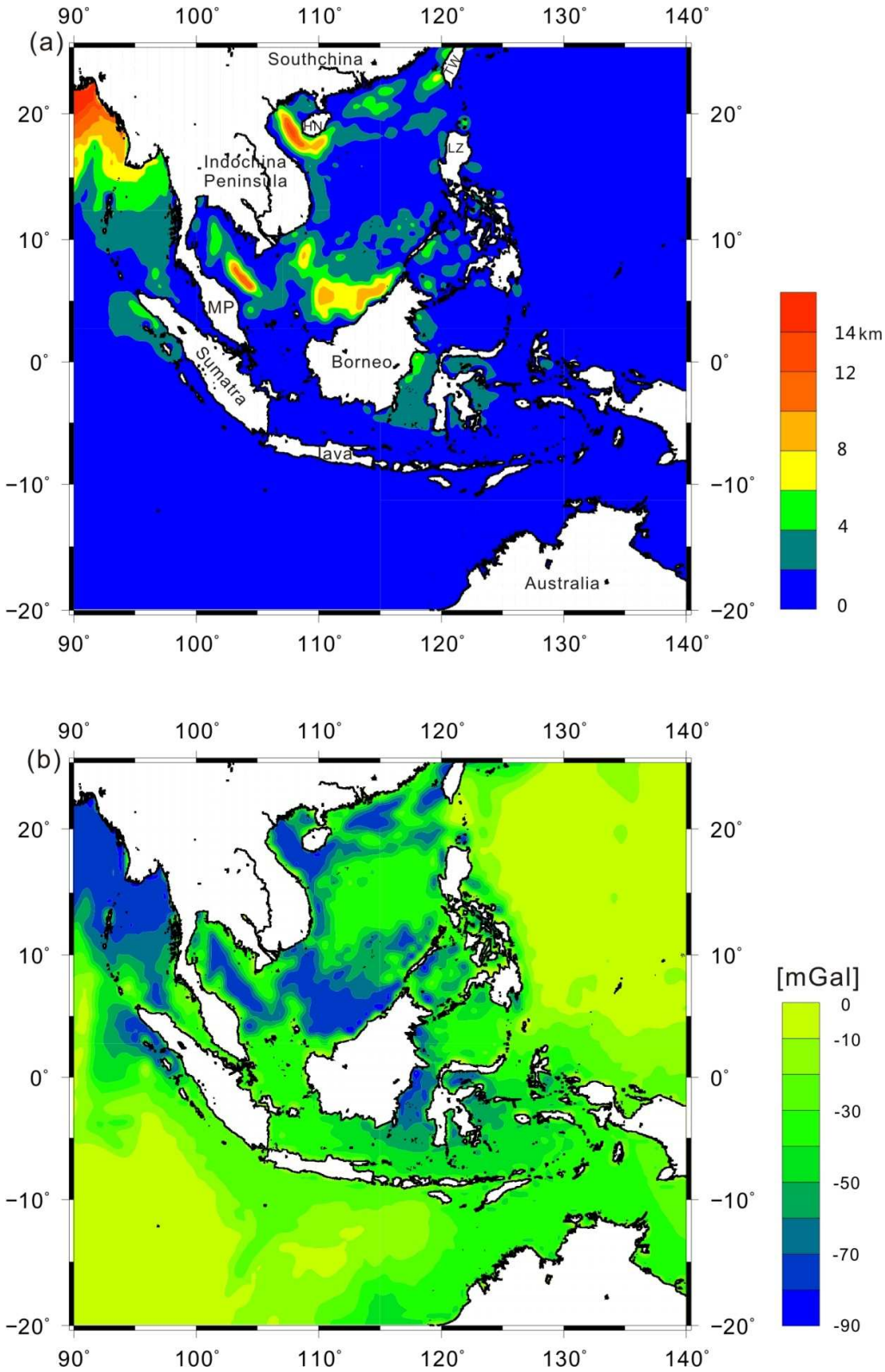

Fig. 3. (a) Sediment thickness and (b) the relative negative gravity anomaly in SE Asia. Abbreviations: MP, Malay Peninsula; HN, Hainan Island; TW, Taiwan Island; LZ, Luzon Island.

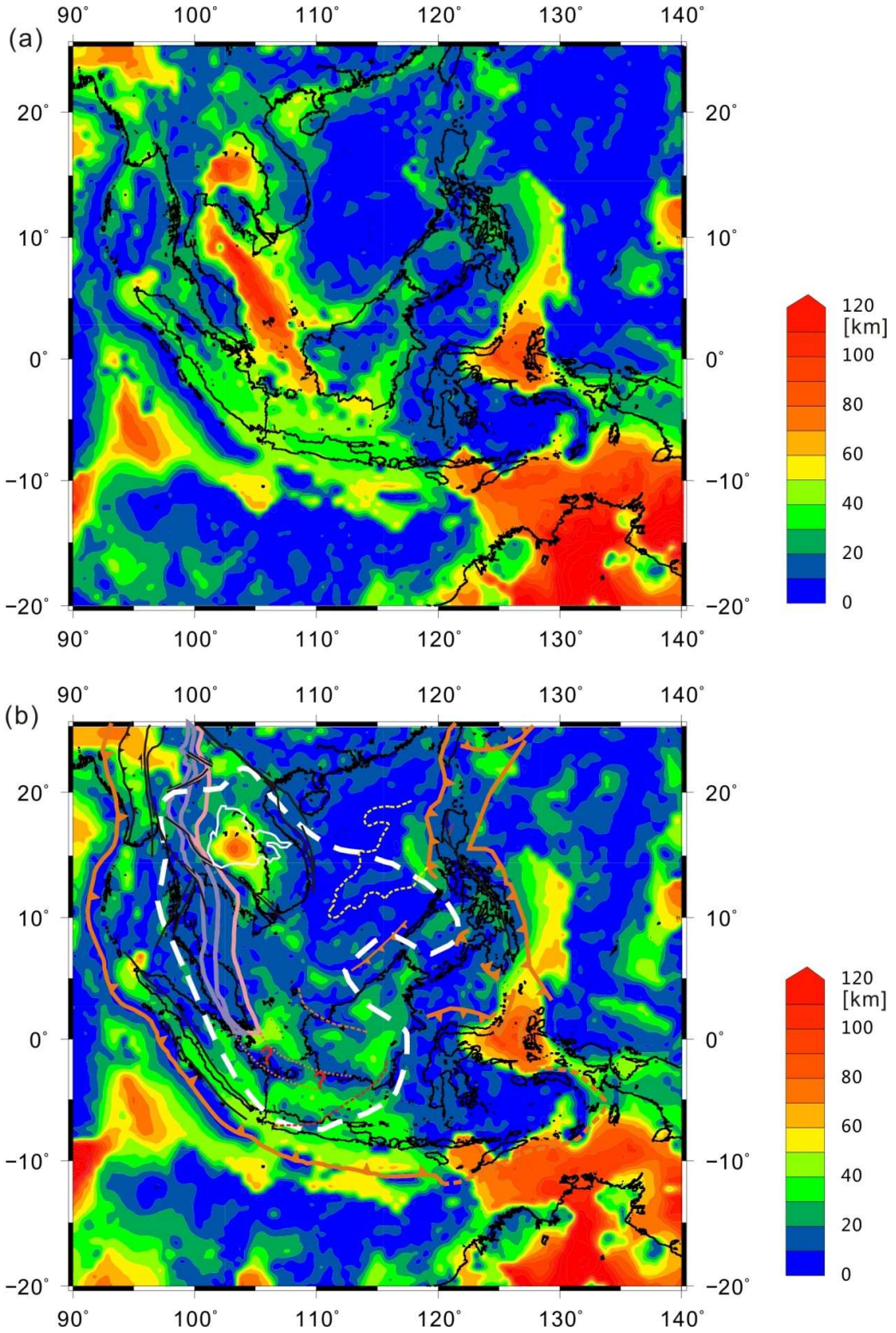

Fig. 4. T_e estimates from $|\mathbf{k}_0|$ = 2.668 in SE Asia. (a) Sediment-uncorrected; (b) sediment-corrected. The yellow dashed curve shows the ocean-continent boundary of the South China Sea. Tectonic

lines are the same as for Fig. 1 (Some in different color for readability).

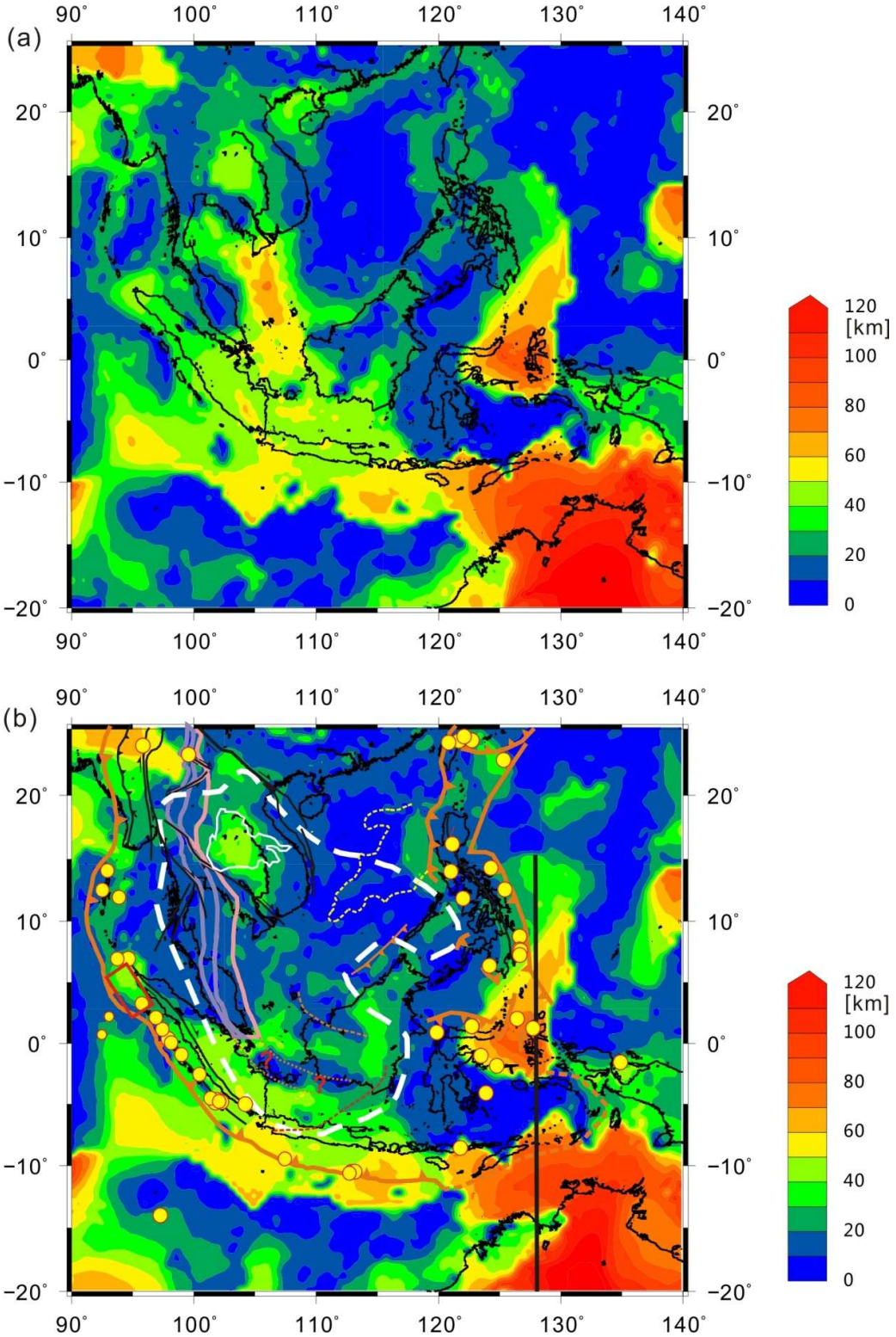

Fig. 5. T_e estimates from $|\mathbf{k}_0|$ = 3.773 in SE Asia. (a) Sediment-uncorrected; (b) sediment-corrected.

The yellow dashed curve shows the ocean-continent boundary of the South China Sea. Yellow solid points refer to earthquakes (Ms> 7.0, www.isc.ac.uk), and the great historic earthquakes in the Sundasubduction system (Sumatra and Java trenches) (Grevemeyer and Tiwari, 2006). The red quadrilateral region over the northwest of Sumatra shows the large rapid slip region of the Sumatra-Andaman earthquake that occurred in December 2004 (M = 9.3) (Shapiro et al., 2008). Tectonic lines are the same as for Fig. 1 (Some in different color for readability).

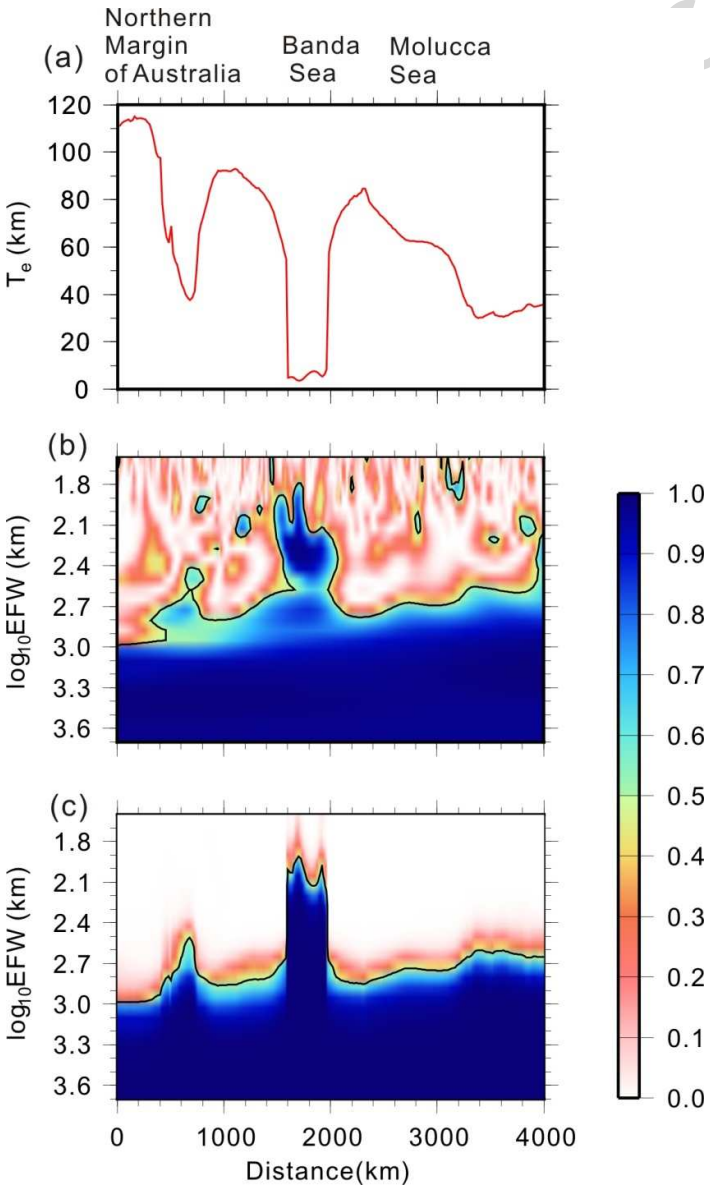

Fig. 6. Cross sections along the profile shown in Fig. 5, from south to north. (a) T_e (km); (b) observed Bouguer squared real coherency (SRC); (c) predicted Bouguer SRC. The black contour in (b) and (c) is SRC = 0.5. EFW on the ordinate in (b) and (c) is equivalent Fourier wavelength.

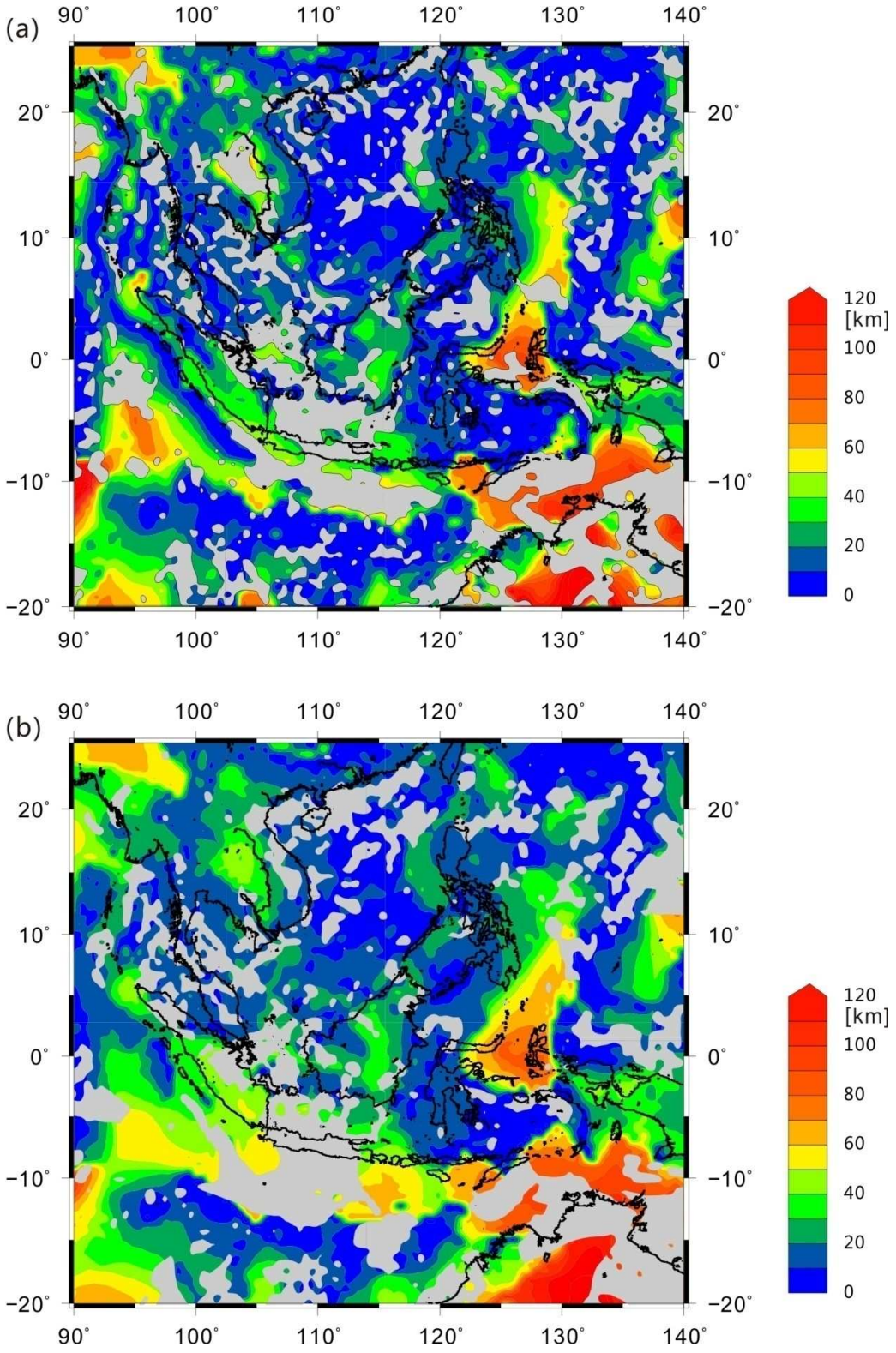

Fig. 7.Sediment-corrected T_e estimates in SE Asia with regions of the maximum value of the normalized free-air SIC $\overline{T}^2_{F,I} > 0.5$ masked in grey. (a) $|\mathbf{k}_0|$ = 2.668; (b) $|\mathbf{k}_0|$ = 3.773.

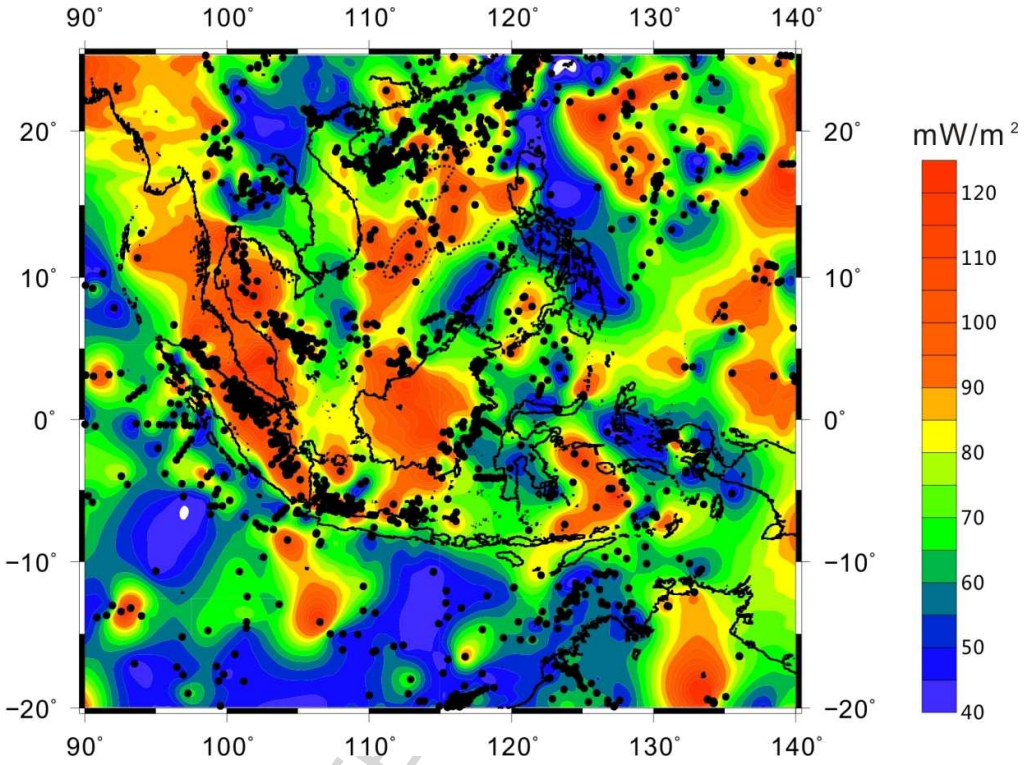

Fig. 8. Regional surface heat flow in SE Asia. The heat flow data in the South China Sea are collected from Shi et al. (2003) and recent contributions. The heat flow data in the adjacent area of the South China Sea are from the updated global heat flow database of the International Heat Flow Commission. To be noted, because of the limited heat flow data set, and their extremely uneven distribution, the heat flow map, which is drawn directly based on the data set, is not always reliable, and might be fraudulent and misleading in the regions with few or no heat flow stations.

.

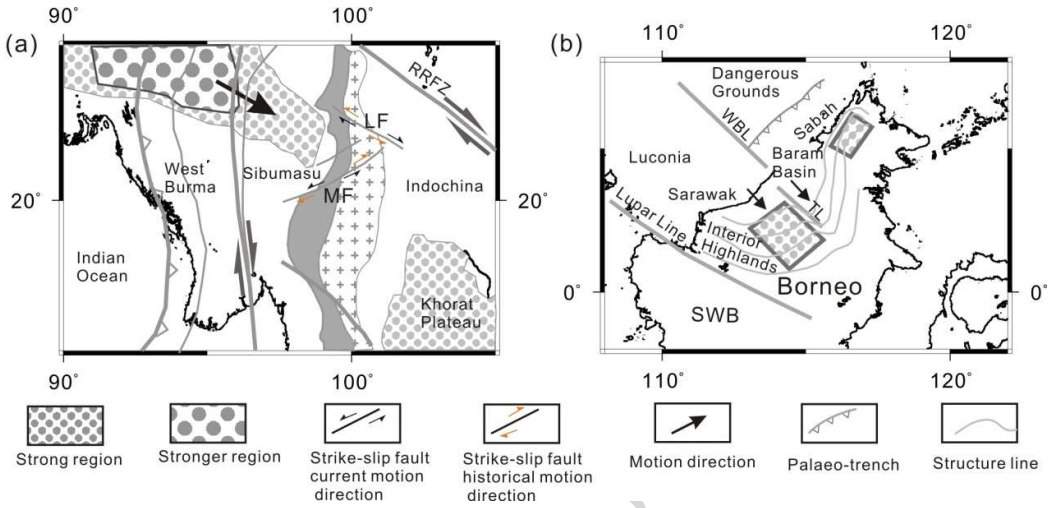

Fig. 9. Schematic diagrams of rigid bodies influencing local deformation. LF, Lancang strike-slip fault; MF, Mengxing strike-slip fault; RRFZ, Red River Fault Zone; WBL, West Baram Line; TL, Tinjar Line.

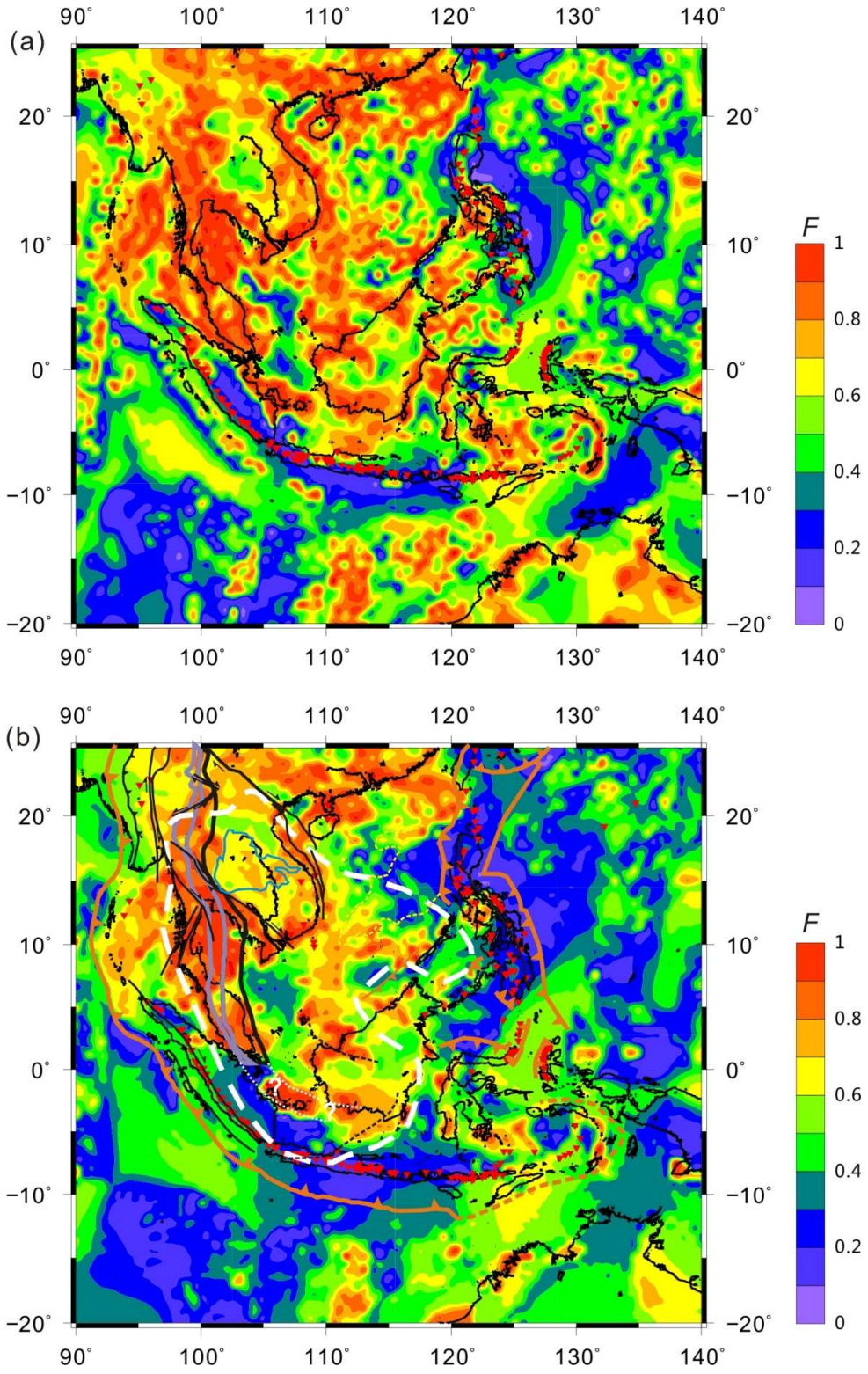

Fig. 10. Internal load fraction, F, corresponding to the above recovered T_e. (a) $|\mathbf{k}_0| = 2.668$; (b) $|\mathbf{k}_0| = 3.773$. The red triangles denote Holocene volcanoes from the Global Volcanism Program (http://volcano.si.edu/). Tectonic lines are the same as for Fig. 1 (Some in different color for

readability).

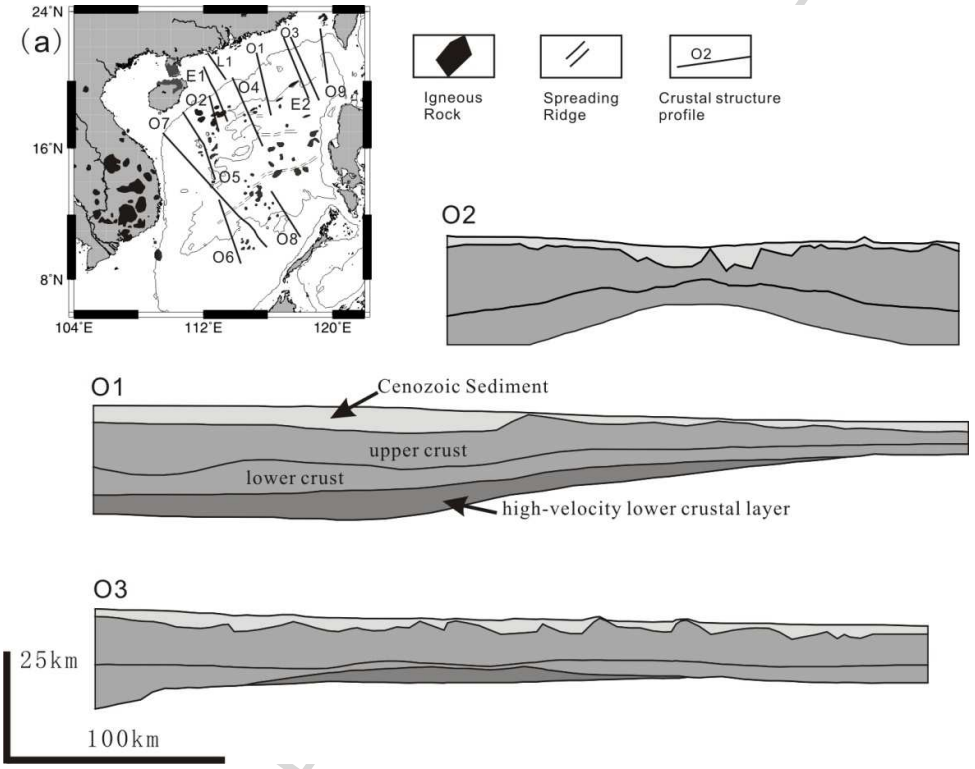

Fig.11. Crustal structure sections (O1, O2 and O3) based on deep seismic data through the continental margins of the South China Sea. Inset (a) shows the locations of these sections.

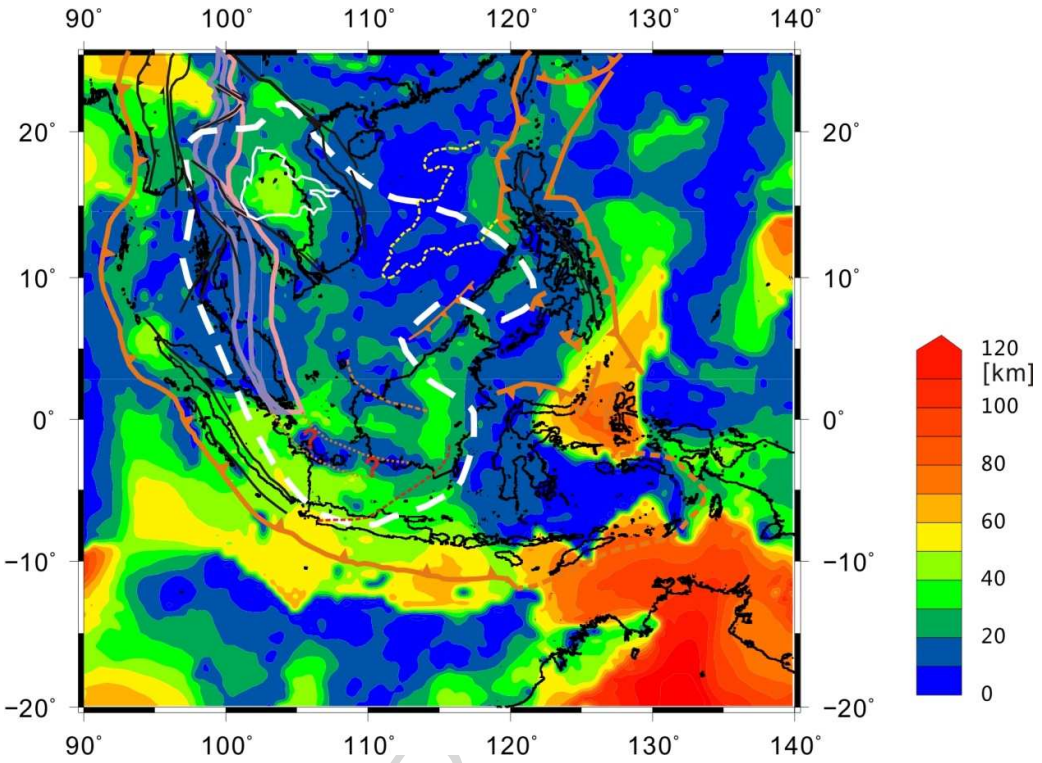

Graphical abstract

Highlights

High-resolution maps of T_e in SE Asia are presented using wavelet methods.

The sediment-corrected T_e maps are more reasonable than uncorrected Te maps.

The heterogeneous strength features are consistent with the complex assemblage of different tectonic units, and significant Cenozoic deformation.

Several isolated stronger regions bounded by low T_e regions in the interior of SE Asia, which help to understand the Cenozoic tectonic deformation in SE Asia.

T_e patterns provide clues of the possible extension of the some tectonic blocks and boundaries.

High internal load fraction F features agrees with the distribution of a high-velocity lower crustal layer and Late Cenozoic basaltic rocks.